12-5-2019

Transmission and Reflection Imaging of Stratigraphy From Passive Array Data

Chloe Olivia Glover

TRANSMISSION AND REFLECTION IMAGING OF STRATIGRAPHY FROM PASSIVE ARRAY DATA

by

Chloë Olivia Glover

A Thesis

Submitted in Partial Fulfillment of the

Requirements for the degree of

Master of Science

Major: Earth Sciences

The University of Memphis

December 2019

DEDICATION

"Now [she] has departed from this strange world a little ahead of me. That means nothing. People like us, who believe in physics, know that the distinction between past, present, and future is only a stubbornly persistent illusion."

-Albert Einstein

This thesis is dedicated to the memory of my grandmother, Barbara Ann Decker. My grandmother moved from Colorado to Washington State in the 1950s, and eventually married my grandfather there. She raised four children in Monroe, Washington, including my father. Growing up in Washington State allowed me to experience earthquakes, hike volcanoes, and helped foster a love of the outdoors. Through each and every turn in my life, my grandmother was quick to encourage me and congratulate me on my accomplishments. Even in baking, where her skills were far superior. My grandmother was always very proud of my siblings and I, often saying that she likes to think some of our smarts came from her, but she didn't want to take any of the credit! Her kind soul was taken from our family much too soon and she will be fondly remembered and sorely missed.

ACKNOWLEDGMENTS

This work seemed impossible at times, and took much support and encouragement from family, friends, and faculty to push through and complete. Now that I'm at the finish line, I'd like to thank all those who helped me get here. I truly couldn't have succeeded without the constant support of my parents, Richard and Barbara Glover. They both pushed me as a child and let me know that I could accomplish anything that I set my mind to.

I need to thank my El Pasoan friends Samantha Ramirez, Erik Day, and many more who coached me through my undergraduate degree at The University of Texas at El Paso, and remained by me through my graduate degree! My friends and classmates at the Center for Earthquake Research and Information including Arushi Saxena, Elizabeth Gilmour, Peter Matheny, Oluwaseyi Bolarinwa, Oluwaseun Fadugba, Eric Jambo, and Trevor Satterfield were amazing resources throughout my studies. Each and every person aided me when I was down and took the time to teach me things that I did not know. I couldn't have done it without you. Thank you to my Memphis friends Anna and Ryan McSchuler, Lauren and Sean Roy, and John and Kara Meredith who emotionally supported me through the last few months in Memphis and gave me much needed breaks from my research! Thank you to Ben Hedin and my new Pittsburgh family for cheering me on and supporting me during the final writing process.

I'd also like to thank Eunseo Choi, Christine Powell, Chris Cramer, Jer-Ming Chiu, Randy Cox, Eric Daub, and Mitch Withers for teaching me the concepts of geophysics and seismology and working with me toward this goal. Finally, thank you to Chuck Langston for believing in me when it seemed no one else did, not even myself. I never would have gotten here

if not for you. Your kindness and understanding are beyond what I deserved, and I am so thankful that you chose to help me achieve this goal.

ABSTRACT

The IRIS Consortium conducted an experiment in Oklahoma in the summer of 2016 using a 3-line array originally intended for a reflection survey. We identified phase conversions in the crust with passive seismic sources. A major Sp phase conversion was identified at 0.5 km, with several other large conversions evident between ~1.5 and 2.5 km depth across all profiles and events. The 0.5 km depth conversion correlates to the base of the Permian red-bed sandstones and shales and the top of the Pennsylvanian limestones/shales/sandstones. The conversions between 1.5- and 2.5-kilometers depth correspond to the top of the Cambrian granites and the Pre-Cambrian basement. Synthetic seismograms were used to validate the structural imaging results and acceptably produced conversions at 0.5 and 1.5-2.5 km depth for a hypothetical strike-slip event. The final results demonstrate that passive arrays installed at dense receiver spacing can reliably image crustal stratigraphy in the absence of active-sources.

TABLE OF CONTENTS

Chapter		Page
	List of Tables	ix
	List of Figures	x
1	Geology and Seismicity	1
	Introduction	1
	Geologic Setting	5
	Oklahoma Seismicity	10
2	Data and Methods	11
	The IRIS Community Wavefield Experiment	11
	Seismic Sources	13
	Velocity Model	14
	Data Processing and Methods	18
3	Results and Discussion	26
	Vertical Resolution	26
	Polarity Reversals	27
	Sp Conversion in N-S and W-E Profiles	28
	Synthetic Seismograms	33
	Correlating Discontinuities in Time and Depth	35
4	Conclusions	39
	Conclusions	39
5	References	41

Appendices

A. Additional Tables 44

B. Supplementary Figures 48

LIST OF TABLES

TABLE		PAGE
Table 1	Earthquake Source Information	15
Table 2	Depth-Migration Processing Steps	18
Table 3	Vertical Resolution	26
Table 4	Number of Events by Depth	38

SUPPLEMENTARY TABLES

Table A1	Kirk 1985 Sonic Log Velocity Model	45
Table A2	1D Combined Velocity Model	49

LIST OF FIGURES

FIGURE		PAGE
Figure 1.1.1	RTZ Seismogram with Sp Arrivals, Event 1, Station 1041	1
Figure 1.1.2	Sp Conversions in the Crust	3
Figure 1.2.1	Oklahoma Geologic Provinces	7
Figure 1.2.2	Geologic Map of Oklahoma	8
Figure 1.2.3	Northern Oklahoma West-East Cross Section	8
Figure 1.3	Stratigraphic Column from Well Logs	9
Figure 1.4	Oklahoma State Seismicity: 2005-2015	10
Figure 2.1	IRIS Community Wavefield Experiment	12
Figure 2.2	1D Velocity Model	14
Figure 2.3	Smoothed Velocity Model	17
Figure 2.4	S-to-P and S-minus-Sp Travel Time Curves, Event 1, Line 1000	20
Figure 2.5	Event 1: Pre-Processed, Time Reversed, and Depth-Migrated Data	21
Figure 2.6	Event 1: Depth Migrated Images, Line 1000, 2000, & 3000	22
Figure 2.7	Testing the Depth and Velocity Model	23
Figure 2.8	Processed Synthetic Seismic Data	25
Figure 3.1	P-wave Polarity Reversal—Event 5	27

Figure 3.2 Cut and Linked Depth-Migrated Images from Event 2 29

Figure 3.3 Event 5, Lines 1000, 2000, and 3000—Depth Adjusted 32

Figure 3.4 Synthetic Seismograms at Different Source Depths 34

Figure 3.5 Event 1: Depth-Migrated Images—Phases Labeled 36

SUPPLEMENTARY FIGURES

A1 Event 1, Original Processed Images 49

A2 Event 2, Original Processed Images 52

A3 Event 3, Original Processed Images 55

A4 Event 4, Original Processed Images 58

A5 Event 5, Original Processed Images 61

Chapter 1—Geology and Seismicity

Introduction

The 2016 IRIS Oklahoma Wavefield Experiment short-period array recorded 270 seismic events in 30 days while deployed near Enid, Oklahoma. Of those events, 20 had magnitudes greater than or equal to ml 1.50. Computed depths of these earthquakes range from 1.2 km to 5.2 km (Sawi & DeShon, 2017). The geometry of the short-period passive array was originally designed for a vibroseis-source experiment, which uses a truck-mounted active-source

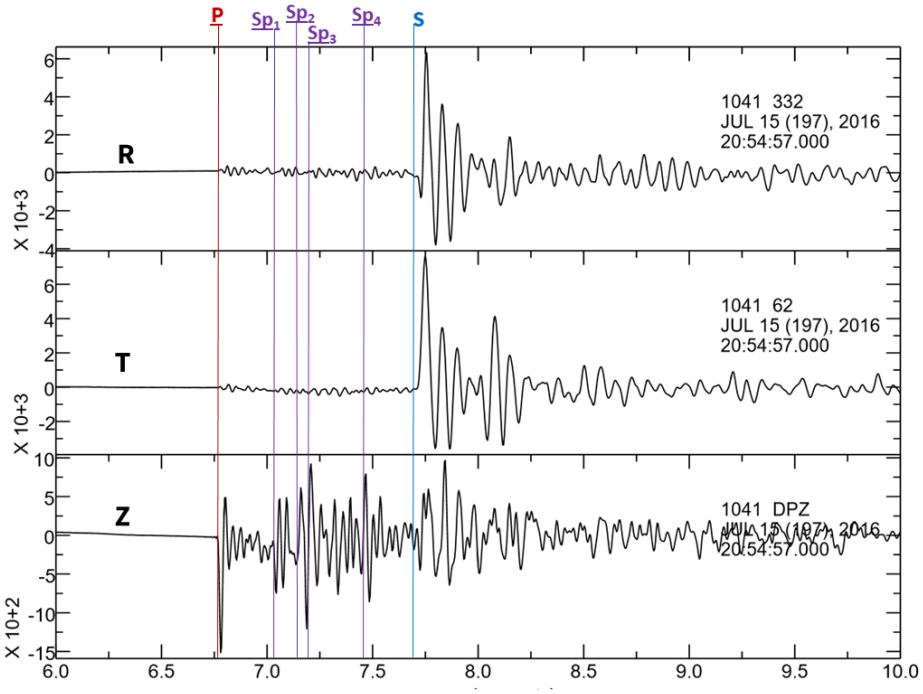

Fig. 1.1.1: *Radial, transverse, and vertical (R, T, Z) components of Event 1 recorded at station 1041. The earthquake was ml 2.28 with a 5.28 km hypocentral depth (see Table 1). Arrival of the P-wave, four large Sp conversions, and the S-wave are indicated by the red, purple, and blue lines respectively.*

instrument that produces seismic waves with an oscillating mass (Sheriff, 2002), though the source was never used. The high-density placement of the receivers allowed for accurate hypocenter locations (depth errors <0.5 kilometers), magnitude calculations of the shallow earthquakes beneath the array (Sawi & DeShon, 2017), and maximum resolution and minimal aliasing (Anderson et al., 2016; Sweet et al., 2018). It also gave us the unique opportunity to use passive-source waveforms in the recorded seismograms at each station to identify crustal discontinuities via Sp conversions and image the upper crustal structure beneath the array (Bath & Stefánsson, 1966; Bock & Ha, 1984; Li et al., 2018). As S-waves travel from a source to a receiver, they can convert to P-waves at discontinuities in the crust. This type of phase conversion is called an Sp conversion (Bath & Stefánsson, 1966; Fig. 1.1.1; Fig. 1.1.2). P-waves can also convert to S-waves at velocity contrasts, but this type of wave conversion will not be used in our study. Sp conversions from discontinuities nearest the source will be recorded on a seismogram soon after the P-wave, and Sp conversions from discontinuities nearest the surface will be recorded immediately before the S-wave arrival. All Sp conversions created by discontinuities between the source and receiver will arrive between the P-wave and S-wave arrivals (Bath & Stefánsson, 1966; Smith, 1970). Fig. 1.1.1 highlights four clear Sp conversion arrivals (shown in purple) on the vertical component between the P- and S-wave arrivals, and Fig. 1.1.2 illustrates the wave behavior at velocity contrasts, and the resulting Sp and Ps conversions.

Our study area in northernmost Oklahoma near 37° latitude is characterized by pre-Cambrian crystalline basement overlain by relatively undeformed layers of Paleozoic sedimentary rocks that range in thickness from ~800 meters near the Ozark Uplift to 3 kilometers

in the Anadarko shelf. The two major structures across this section of Oklahoma are the Nemaha Uplift and the Cimarron Arch; both modern-day extensional features (Gianoutsos et al., 2014; Johnson, 2008; Fig. 1.2.1). Seismically, this region is historically quiet, but has experienced a sharp increase in frequency of events in recent years (Darold et al., 2015; Keranen et al, 2014; McNamara et al., 2015). Many oil and gas fields exist in the state of Oklahoma and wastewater injection sites likely produced the earthquakes recorded by the experiment (Boyd, 2002; Chen et al., 2017; Ellsworth, 2013; Keranan et al., 2014).

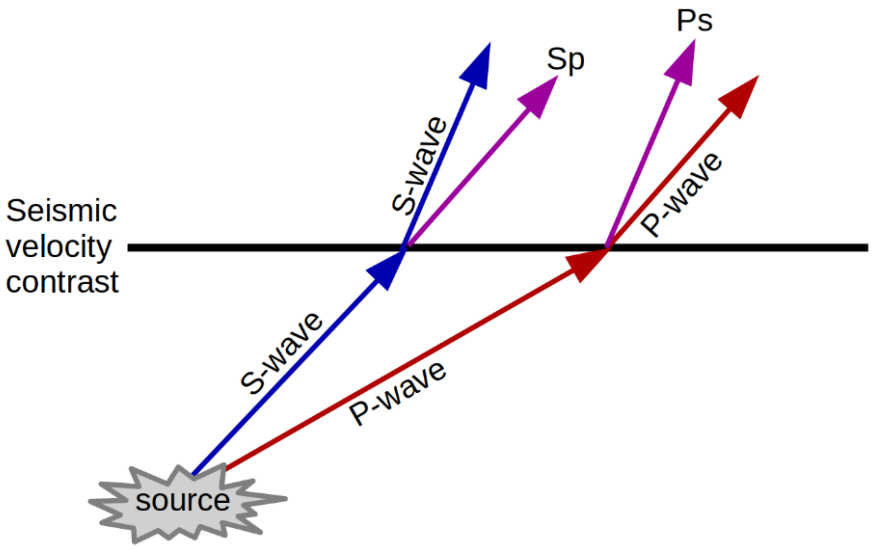

Fig. 1.1.2: *Sp conversions in the crust. S-waves (blue) and P-waves (red) crossing crustal discontinuities can convert to P-waves and S-waves, respectively. An S-wave converting to a P-wave is an Sp conversion, and a P-wave converting to an S-wave is a Ps conversion.*

A 1985 compensated sonic log from the Mobil Oil Corporation (Kirk, 1985) combined with a crustal model from the 2014 Oklahoma Geological Survey Earthquake Summary Report (Darold et al., 2015) was used to construct the initial velocity-depth model. A smoothed version of this velocity model was used for processing, forward modeling, and production of synthetic

seismograms. Initial P, S, and Sp travel time estimates were calculated using ray theory. Seismic data pre-processing for each event included synchronizing the 3-component data, obtaining a time window, correcting for instrument response, and rotating the N and E components to radial and transverse. Next, the data were grouped by receiver line and processed by treating each linear group of seismic stations as an individual array. Finally, we compute an Sp conversion record section for each temporary linear (Baysal et al., 1983; Kirk, 1985). This technique is similar to receiver function analysis in that it uses the frequency content of an incoming wave to model the structure beneath the seismometer. However, receiver functions use Ps conversions of wave reverberations to image structure rather than Sp conversions, and analysis requires three components to isolate the receiver response via deconvolution of the vertical response from the radial response in a plane-layered structure (Langston, 1979). Receiver function studies are often completed with teleseismic events rather than local earthquakes and have the potential to produce high resolution images.

Vertical resolution is often defined as one quarter of the wavelength; wavelength is the velocity divided by the dominant frequency. Low velocities and high frequencies result in increased vertical resolution, while high velocity and low frequency result in poor resolution. Active-sources can produce higher frequencies than natural earthquakes. The Vibroseis, which was originally intended as the source for the short-period array used in this study, can produce frequencies between 60 and 235 Hz (Sheriff, 2002). A Vibroseis survey with a 5 km/s seismic wave velocity and a 60 Hz frequency will have a 20 m vertical resolution. However, the resolution will decline with increasing depth (Rafaelsen, 2012). Obviously, shallow, local, passive seismic sources will not have a dominant high-frequency content. Our dominant

frequency in this study ranges from 5-20 Hz over the five events and three seismic lines, though higher frequencies are present in the data and can improve the vertical resolution. We cannot image a single very-thin (20 m) layer of strata but we can resolve layers with thicknesses of 73 meters or greater (Rafaelsen, 2012). This vertical resolution is more than sufficient to identify large seismic velocity contrasts and correlate them to known stratigraphic boundaries. Moreover, the ability to image large crustal structures with natural seismic sources in a local array without needing expensive active-sources like Vibroseis, dynamite, etc., that require extensive prep-work and permitting is advantageous.

Geologic Setting

The geology of Oklahoma is marked by two large depositional and structural Paleozoic sedimentary basins in central and southern Oklahoma: the Arkoma Basin to the southeast, and the 12-kilometer-deep Anadarko basin to the mid-west of the state (Johnson et al., 2000; Perry, 1989; Johnson, 2008; Fig. 1.2.1). Both basins are flanked by the following Pennsylvanian aged uplifts: the Ouachita to the southeast, the Wichita to the southwest, the Ozark to the east, and the Arbuckle in south-central Oklahoma (Johnson, 2008; Johnson et al., 2000; Fig. 1.2.1; Fig. 1.2.2). Oklahoma's oldest rocks are 1.4 Ga granites and gneisses which were overlain by Cambrian rhyolite, gabbro, and basalt ~515 Ma in southwest and south-central Oklahoma (Johnson, 2008; Perry, 1989; Fig. 1.2.2). Basement rocks are at approximately 0.3 kilometers depth in the Ozark uplift and 9-12 kilometers depth in the Arkoma and Anadarko sedimentary basins (Johnson, 2008; Fig. 1.2). Basement exposure has been mapped in the Wichita and Arbuckle Mountains (Perry, 1989). During the late Cambrian to Ordovician, Pre-Cambrian deposits were eroded over

the eastern and southeastern parts of the state. Limestone, dolomite, and sandstone covered the majority of Oklahoma while the Arbuckle group, mostly limestone and dolomite, increased in thickness southward (Johnson, 2008; Perry, 1989). The limestone deposits from this time contained early marine invertebrates such as trilobites, brachiopods, and bryozoans. In the Ordovician, limestone with layers of sandstone and shale were deposited, along with dolomite with maximum thickness of 300 meters which was partially eroded and then overlain by black shale, chert, and sandstone. Widespread uplift in the early Mississippian prompted erosion, and shallow seas in the northern part of the state allowed for the deposition of the thick Mississippi limestones (Johnson, 2008; Johnson et al, 2000; Fig. 1.2.4). During the Pennsylvanian, major uplift occurred in Oklahoma as well as subsidence of notable sedimentary basins during two crucial orogens. The first of these deformation events is the Wichita orogeny which uplifted the Wichita mountains, and the second is the Ouachita orogeny which was active as a northward-moving fold and thrust belt (Johnson, 2008; Johnson et al., 2000). In the Mesozoic, sediments were carried and deposited in basins from east to west. The Cretaceous was dominated by another shallow sea that extended into Oklahoma, and contributed to the deposition of more sandstones, shales, and limestones (Johnson, 2008; Fig. 1.2.4). In the Tertiary Period, terrestrial deposition direction shifted and sediments were deposited from west to east. The last ice age (~11.5 ka) created a massive drainage system as glaciers retreated and shaped Oklahoma through fluvial processes (Johnson, 2008).

North Central Oklahoma near the IRIS Oklahoma Full Waveform Experiment site can be described as predominately flat lying strata that increases in thickness to the west and south, and is bounded to the east by the Nemaha Uplift (Anderson et al., 2016; Gianoutsos et al., 2014;

Johnson, 2008; Fig. 1.2.1). At the array site, Paleozoic sedimentary strata appear to dip shallowly and are less than 3 km thick (Johnson, 2008; Fig. 1.2.3). Stratigraphy data from two different wells shown in Fig. 1.3 indicate the ages and thicknesses of relevant rock types in Grant county, OK near the location of the array (Gianoutsos et al., 2014; Fig. 1.3).

Fig. 1.2.1: *Geologic province map of Oklahoma. Study area is located within the red square (from Johnson, 2008)*

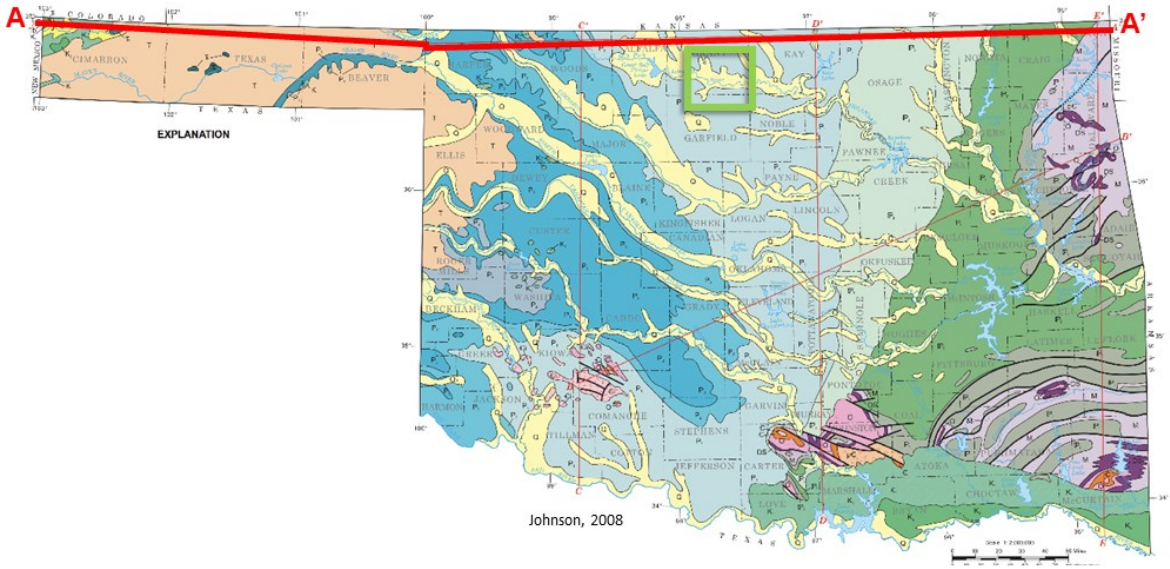

Fig. 1.2.2: *Geologic map of Oklahoma. Study area is located within the green square (from Johnson, 2008)*

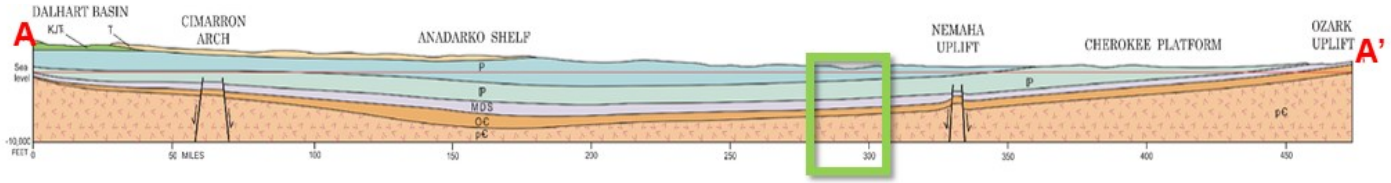

Fig. 1.2.3: Cross section A-A' from Oklahoma Geologic Map in Fig. 1.2.2. Study area shown with green square (from Johnson, 2008)

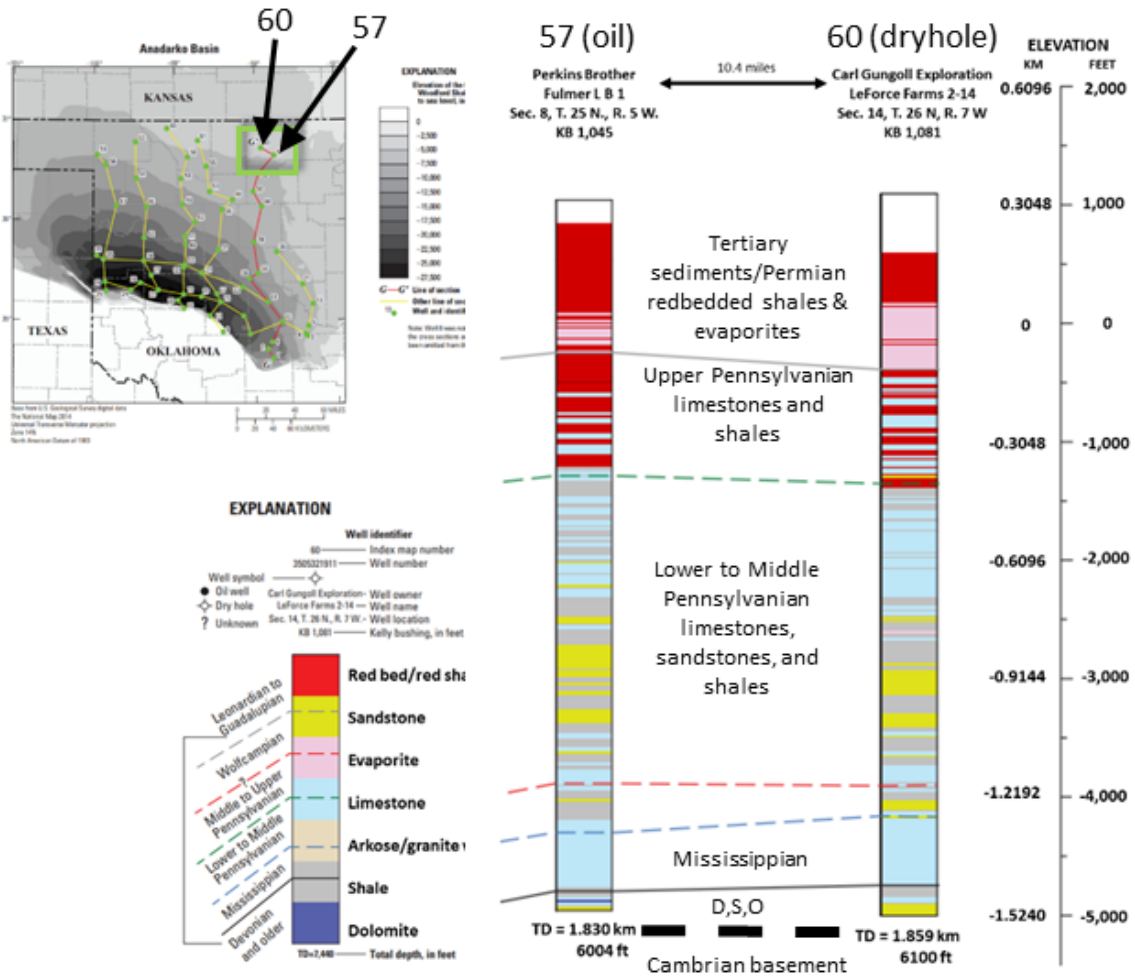

Fig. 1.3: *Lithology from an oil well (57, left) and a dryhole (60, right) in Grant county, Oklahoma (from Chapter 10, plate 7 of Gianoutsos et al., 2014). Array location (green square) and wells 57 and 58 are shown in upper left figure. Stratigraphic boundaries are labeled between the two columns. Rock type key at bottom left.*

Oklahoma Seismicity

Oklahoma is far from any plate boundary, and there are no major active faults mapped in the region directly surrounding the IRIS Community Wavefield Experiment site (Anderson et al., 2016; Marsh & Holland, 2016), yet seismicity in Oklahoma increased relatively consistently since 2009 (Chen et al., 2017; Ellsworth, 2013; Hincks et al., 2018; IRIS, 2018). From 2005 to

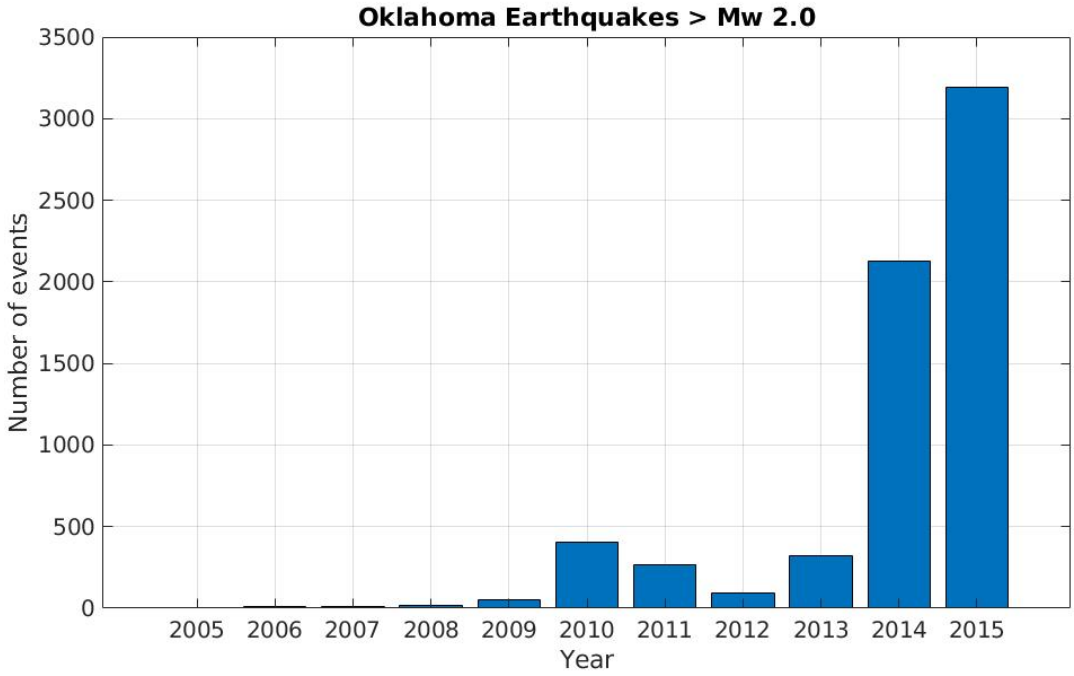

Fig. 1.4: *Oklahoma earthquakes over Mw 2.0 between 2005 and 2015 (IRIS, 2018). See Table 5 for event number values.*

2015, earthquakes of magnitude 2.0 and above increased from 4 earthquakes in 2005 to 3,193 earthquakes in 2015 (IRIS, 2018; Fig. 1.4). An earthquake can be triggered by increasing shear stress, decreasing normal stress, or increasing pore pressure. Hydraulic fracturing, wastewater injection, and other processes can alter the pore pressure and stress of a rock at depth via a pressure front, or even change the load on a fault without initially fracturing it, which releases

stress and energy in the form of an earthquake (Ellsworth, 2013; Holland, 2013; McGarr et al., 2002). Of the 270 events that occurred within and near the bounds of the IRIS Community Wavefield Experiment, 189 were between 3.0 and 5.5 km depth (Sawi & DeShon, 2016), while oil and gas wells in northern Oklahoma that are drilled to the crystalline basement have maximum depths averaging 1.6-2.4 km according to publicly available OK well data (Campbell, J.A., 2003). There were just 5 events in the array that occurred at 2.5 km depth or shallower (Sawi & DeShon, 2016), which indicates that the faults that are being activated and causing seismic events are at greater depths than the maximum well depths and do not require a direct hydrologic link; thus, the change in mass and volume above the fault changes the normal stress and shear stress and is enough to activate the fault (Ellsworth, 2013; McGarr et al., 2002). Much of the seismic activity near the array has been attributed to wastewater injection sites, and has resulted in more seismic activity in Oklahoma than all other states in the contiguous United States (Hincks et al., 2018; Holland, 2013).

Chapter 2—Data and Methods

The IRIS Community Wavefield Experiment

The IRIS Community Wavefield Experiment included 4 main components: a 7-layer nested gradiometer, an 18 broadband station Golay array, 9 infrasound stations, and 3 seismic lines, all located northeast of Enid, OK in Grant county (Anderson et al., 2016). See Fig. 2.1 for array geometry, all local earthquake epicenter locations during the 30-day experiment, and location and depth of the 5 processed events (Anderson et al., 2016; Sawi & DeShon, 2016). For the fourth listed experiment in the Oklahoma community wavefield project, 247 three-

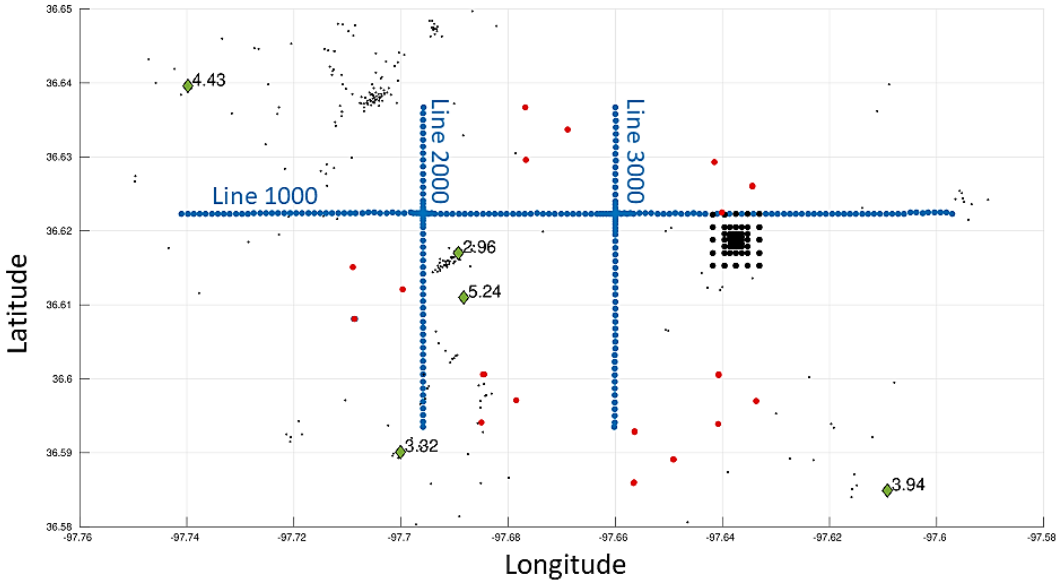

Fig. 2.1: *IRIS Community Wavefield Experiment Array. This work uses the 3-component short-period array arranged in 3 seismic lines. The two north-south blue lines are approximately 4.8 km long. The western line is "line 2000", and the eastern line is "line 3000". The east-west blue line is approximately 13 km long and referred to as "line 1000". All 270 recorded events are shown with small black markers. Processed event locations are indicated by green diamonds and are labeled with their respective depths. Event 1: 5.24 km, Event 2: 4.43km, Event 3: 3.94 km, Event 4: 3.32 km, and Event 5: 2.96 km. See* Table 1 *for detailed earthquake information.*

component short period stations were deployed from June 30 through July 30, 2016 with a sample rate of 250 samples/second and a 12 dB gain. The stations were arranged in two seismic lines (each 4.8 km long) running north-south, and one line (13 km long) running east-west. The E-W line will be referred to as line 1000, the western and eastern N-S lines will be referred to as line 2000 and line 3000, respectively (see Fig. 2.1). The nodes were spaced 100 meters apart, with higher density (as close as 33 m) node spacing at the intersection of N-S and E-W lines (Anderson et al., 2016; IRIS, 2016; Sweet et al., 2018; Fig. 2.1). The array was initially intended for a Vibroseis reflection survey, but this survey did not happen. The purpose of the wider IRIS

experiment was to observe full waveforms using arrays designed to allow easy detection and location of events, and to allow for robust imaging of the collected data by acting as a high-density regional array with high resolution and low aliasing (Anderson et al., 2016; Sweet et al., 2018). Our purpose is to use a passive array to determine the maximum resolution, correlate Sp conversions with known stratigraphy, and test if our results are real and reproducible by creating synthetic seismograms and testing the data.

Seismic Sources

The IRIS Oklahoma Wavefield Experiment 3-component short-period receivers recorded a total of 270 local earthquakes with a maximum magnitude of ml 2.95, and depth ranges between 0.5 km and 7.2 km (Anderson et al., 2016; IRIS, 2016; Fig. 2.1). Three high density clusters of seismic events are evident to the south of line 2000, to the northwest of line 2000, and to the southeast of the cross-hairs of lines 2000 and 1000 (IRIS, 2016; Sawi & DeShon, 2016; Fig. 2.1). For the purpose of imaging the stratigraphy beneath the array, events with source depths of ~3.0 km or greater were used. The five events of interest were chosen based on their depths, magnitudes, and epicenter location. They are indicated by green diamonds on Fig. 2.1 and labeled with their original source depths in kilometers. Events are named as 1 through 5, and their respective catalog depths in kilometers are 5.24, 4.43, 3.94, 3.32, and 2.96 (IRIS, 2016; Sawi & DeShon, 2016; Fig. 2.1; Table 1). All events used in this study occurred between the 8th and 16th days in July of 2016. Events 2 and 3 are located to the far northwest and far southeast corners of the array, and were specifically chosen to determine if seismic waves are affected by local structure and discontinuities differently if they originate from different directions; that is to say, are they directionally dependent? Events 1 and 5 are both proximal to the western cross-

hairs (the intersection of lines 1000 and 2000) and vary greatly in depth (5.24 km versus 2.96 km). Event 4 is located at the southernmost point of line 2000, and has a depth of 3.32 km (IRIS, 2016; Sawi & DeShon, 2016; Fig. 2.1).

Velocity Model

Seismic body waves can be separated into two major types: shear (S) waves and compressional (P) waves. The direction of propagation of a shear wave is perpendicular to the

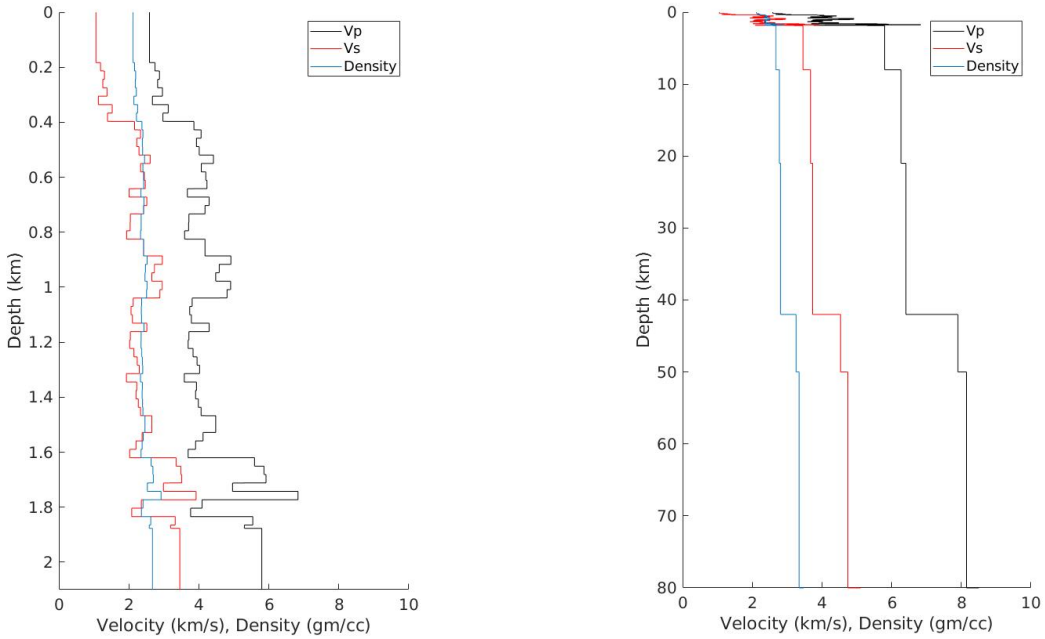

Fig. 2.2: *1D Velocity Model.* Left*: Velocity model calculated from Kirk, (1985) compensated borehole sonic log, up to 2 km depth.* Right*: Kirk, (1985) sonic long combined with generalized earth model after 2 km from the 2014 Oklahoma Earthquake Summary Report (Darold et al., 2015)*

motion of the medium it travels through, while compressional waves propagate in the same direction as the motion of the medium, resulting in P-wave velocities that are ~60% faster than S-wave velocities (Stein & Wysession, 2009). Seismic waves can convert into different phases

TABLE 1: Earthquake Source Information

Event #	Latitude	Longitude	ml	Depth (km)	Year	Mo	Day	HH:MM:SS
1	36.611	-97.6883	2.28	5.2469	2016	7	15	08:55:02 PM
2	36.6396	-97.7398	2.79	4.433	2016	7	8	01:41:55 PM
3	36.5849	-97.6092	0.78	3.9481	2016	7	16	11:47:46 AM
4	36.5901	-97.7001	2.02	3.3284	2016	7	8	08:18:21 PM
5	36.617	-97.6893	2.95	2.96	2016	7	11	05:55:17 AM

when they cross seismic velocity contrasts, or discontinuities, while traveling through the earth (Bath & Stefánsson, 1966; Smith, 1970; Fig. 1.1.2). A discontinuity is defined as any seismic layer boundary in the earth where there is a notable difference in velocity or density on either side of said boundary (Stein & Wysession, 2009; Fig. 2.2). The phase conversion of interest for this study is the Sp conversion. As S-waves travel from a source (earthquake) to a receiver (seismic station), they can convert to P-waves at discontinuities in the crust, and produce an Sp conversion (Bath & Stefánsson, 1966; Bock & Ha 1984; Smith, 1970). See Fig. 1.1.2 for an illustration of Sp and Ps conversions. A seismic station recording the arrival of seismic waves traveling through a homogeneous earth will record the P-wave first, and then the slower traveling S-wave shortly after (Bath & Stefánsson, 1966). If there are discontinuities in the crust, however, we can expect phase conversions (Stein & Wysession, 2009). Sp conversions from discontinuities nearest the source will be recorded after the P-wave, and Sp conversions from discontinuities close to the surface will be recorded before the S-wave arrival. All the resolvable

discontinuities between the source and receiver that are affecting the traveling S-waves will be evident in the seismogram as peaks and troughs between the P-wave and S-wave arrivals (Bath & Stefánsson, 1966). The Sp converted waves have a different travel time than P- and S-waves, and we can calculate the travel times of S-to-P converted waves using geometrical ray theory and a velocity model of the discontinuities in the crust and therefore predict Sp arrivals and waveforms (Bath & Stefánsson, 1966; De Hoop, 1960; Smith, 1970; Stein & Wysession, 2009).

The upper two kilometers of the velocity model used in this study are from a 1985 sonic travel time log from the Mobil Oil Corporation. The well is located in Oklahoma Section 15, Township 26N, Range 7W, and is approximately 22 kilometers northwest of Event 2 used in this study (Kirk, 1985; IRIS, 2016; Fig. 2.1; Table 1). The sonic log was sampled at 100 foot (30.5 meter) intervals. The depth (feet) and travel time (microseconds per foot) were recorded for each interval, starting at 600 feet. We converted all units to S.I. units. To calculate P-wave velocity (V_p), we divided the thickness of the layer (in km) by the difference in transit time (seconds) of the base of the 100 feet section and the transit time at the top of the 100-foot section (Crain, 1984; Kirk, 1985). S-wave velocity (V_s) and density (ρ) were computed using Brocher's relationship between elastic wave-speeds and density, shown in equations 1 and 2 (Brocher, 2005; Table A1).

$$V_p \text{ (km/sec)} = 39.128\rho - 63.064\rho^2 + 37.083\rho^3 - 9.1819\rho^4 + 0.8228\rho^5 \quad (1)$$

$$V_s \text{ (km/sec)} = 0.7858 - 1.2344V_p + 0.7949V^2_p - 0.1238V^3_p + 0.0064V^4_p \quad (2)$$

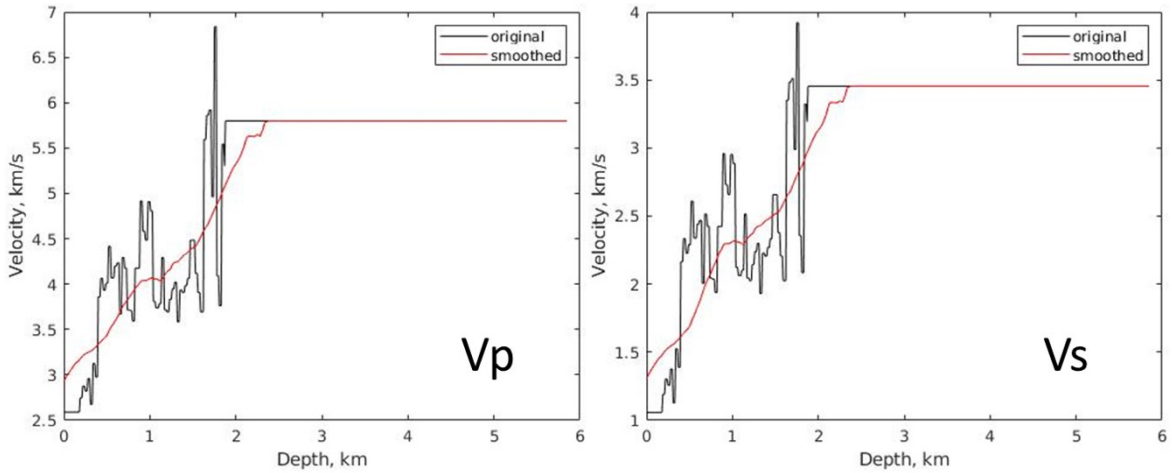

Fig. 2.3: *1D smoothed velocity model for P-waves (left) and S-waves (right).*

The remaining velocity model is from the 2014 Oklahoma Earthquake Summary Report (Darold et al., 2015). See Fig. 2.2 for the full velocity and density model. Once compiled, we smoothed the velocity-depth model so that the small changes reflected in each 100ft/0.03km layer did not influence the travel time calculations, forward modeling, and depth-migration by introducing sharp velocity contrasts (Fig. 2.3). The smoothed model was calculated by sampling the velocity model every 10 meters, and using the average slowness over a depth window (approximately 500 meters above and below each sample location) to find the mean. Without smoothing the velocity model, the travel time plots for S-P and S-Sp will contain visible "steps" when in reality, the travel times are smooth throughout. Fig. 2.4 shows calculated S-P and S-Sp travel times for Event 1, Line 1000. See Table A2 for the full velocity model, and Fig. 2.3 for Vp and Vs original (black) and smoothed (red) velocity-depth models.

Data Processing and Methods

To study the structure of north-central Oklahoma using Sp conversions, we chose five events with epicenters close to the receivers (<12 km radius from center of array) so that the incidence angle is near-normal, and we have greater confidence that the waveforms observed in the data are from the wave's interaction with seismic discontinuities beneath the array. Event information for each earthquake is available in Table 1. Seismic data pre-processing for each earthquake included synchronizing the 3-component data simultaneously for each event by assigning event location and origin time (Sawi & DeShon, 2016) to the SAC (Seismic Analysis Code) files, then obtaining a time window that includes both the P-wave and S-wave arrivals. We corrected for instrument response using the corresponding SAC polezero files after removing the mean, and applying a zero phase, trapezoidal filter with the low frequency taper from 0.05 Hz to 0.5 Hz, and the high frequency taper between 50.0 to 80.0 Hz. The north and east components of each station were rotated to the great circle path to obtain the radial and transverse components. Next, each line of stations (lines 1000, 2000, and 3000) was used to create a separate array (Fig. 2.1), and a text file of pre-processed Z-component SAC files for each station of each new array was compiled for processing. This concludes the pre-processing procedure.

Table 2: Data Processing Steps—Depth Image		
1. FILTER DATA	**Fig. 2.5a**	Highpass two-pole one-pass Butterworth filter with a corner at 2 Hz
2. PICK S-ARRIVAL	**Fig. 1.1.1**	Use the R and T components to pick the S-wave arrival on the Z component

Table 2 (continued)			
3. **TRAVEL TIME & DEPTH MIGRATION**	**Fig.2.4**	I.	Travel time: smooth the velocity model using the average slowness over depth window; calculate shear wave tt for each distance; calculate S-to-P tt for each depth and distance; find difference between S and S-to-P times
	Fig. 2.5b **Fig. 2.5c**	II.	Depth migration: flip seismogram; seismogram stretch—resample time and depth at delta t time increment (1/sampling rate = 0.004)
4. **TEST MODEL**	**Fig 2.7a,d**	I.	*Depth*: Reprocess events that appear to have waveforms "cut off" at the maximum displayed depth. Use a depth deeper and shallower than the catalog depth and re-process from pre-processing to step 1-3.
	Fig. 2.7e	II.	*Velocity model*: Alter the velocity profile by introducing slow or fast discontinuities. Process steps 1-3.
5. **REPROCESS**	**Fig. 2.7**	If tests show that depth or velocity model need to be adjusted, reprocess from pre-processing to steps 1-8.	
6. **SYNTHETIC SEISMOGRAMS**	**Fig. 2.8c**	I.	Produce synthetic seismograms
	Fig. 2.8 a,b,d,e,f	II.	Complete travel time & depth migration. Process from step 1-3.
7. **RESOLUTION CALCULATIONS**	**Table 3**	Use pre-processed and filtered data. Plot the frequency vs amplitude spectra. Identify the dominant frequency in each event and array. Calculate two resolutions ($\lambda/4$ and $\lambda/32$).	

The first step in processing for a depth image is to filter all pre-processed data (Table 2). Radial, transverse, and vertical component SAC files were filtered using a highpass two-pole one-pass Butterworth filter with a corner at 2 Hz to maintain higher frequency signal. Next, the radial, transverse, and vertical components from the seismic station closest to each event epicenter were used to pick and assign S-wave arrival times on the vertical component for each station using the horizontal components as S-wave arrival time references. The station closest to the earthquake will have the shortest travel time. To solve for the travel time of the shear wave and the S-to-P converted wave, we iteratively solve for the ray parameter, p (equations 3, 4, & 5). This is done by using two starting values for the ray parameter, p_1 (zero) and p_2 (use equation

5 for this value), where V_i is the linearly interpolated velocity-depth function of V_p or V_s. We choose a new ray parameter (p_{new}) in each iteration by dividing the sum of p_1 and p_2 by 2. If the change between the p_2 and the p_{new} is below a set tolerance, we accept it as the ray parameter (De Hoop, 1960), and use this value to solve for travel time. If now, we continue to iterate.

$$t = p\,x + \sum d_i\,\eta_i \quad (3)$$

$$\eta_i = (1/V_i^2 - p^2)^{1/2} \quad (4)$$

$$p = 1 / V_i \quad (5)$$

For the above equations, x is the horizontal distance from the epicenter to the receiver, d is the corresponding thickness of each layer from our 1D velocity model, t is the travel time, p is the ray parameter, and V is the corresponding velocity of each layer (Table A2).

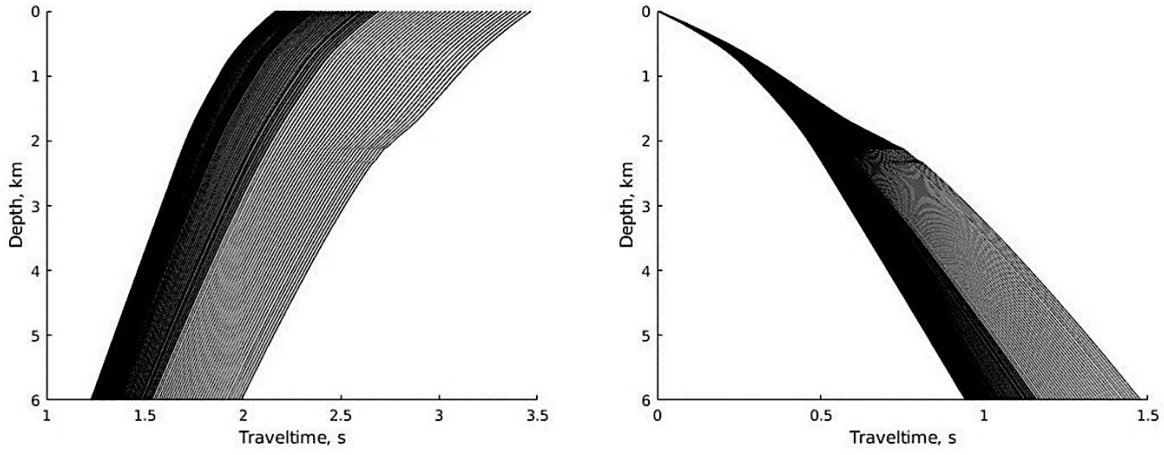

Fig. 2.4: *Travel time curves from Event 1, Line 1000. Left: S-to-P travel time versus depth curve. Right: S minus Sp travel time versus depth curve. Gradient effect is due to close spacing of receivers at line 1000 and 2000 intersections. Travel times are very similar and therefore close together.*

After solving for the ray parameter to calculate travel times (Fig. 2.4), we perform a depth-migration stretch based on our velocity model. We use the S-wave arrival time from the station closest to the event to window the data for all stations relative to the minimum arrival time. Windowing cuts our data from the start of the record to the arrival of the S-wave. The data set is then "flipped" so that the S-wave arrival is plotted at zero time and the P-wave arrival

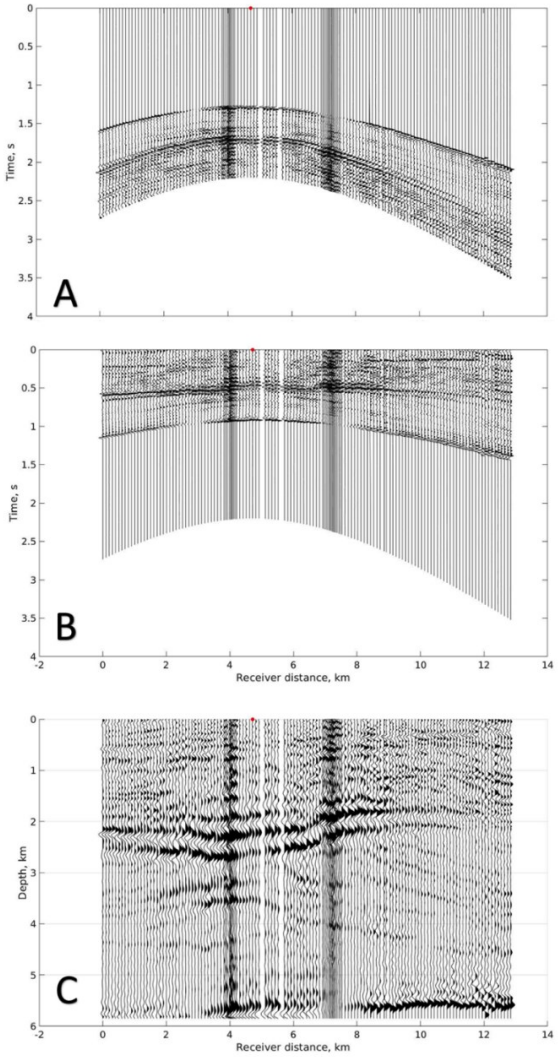

Fig. 2.5: *Event 1, Line 1000. (A) preprocessed and filtered data; (B) time-reversed data; S-wave arrival is at 0 seconds (C) depth-migrated data*

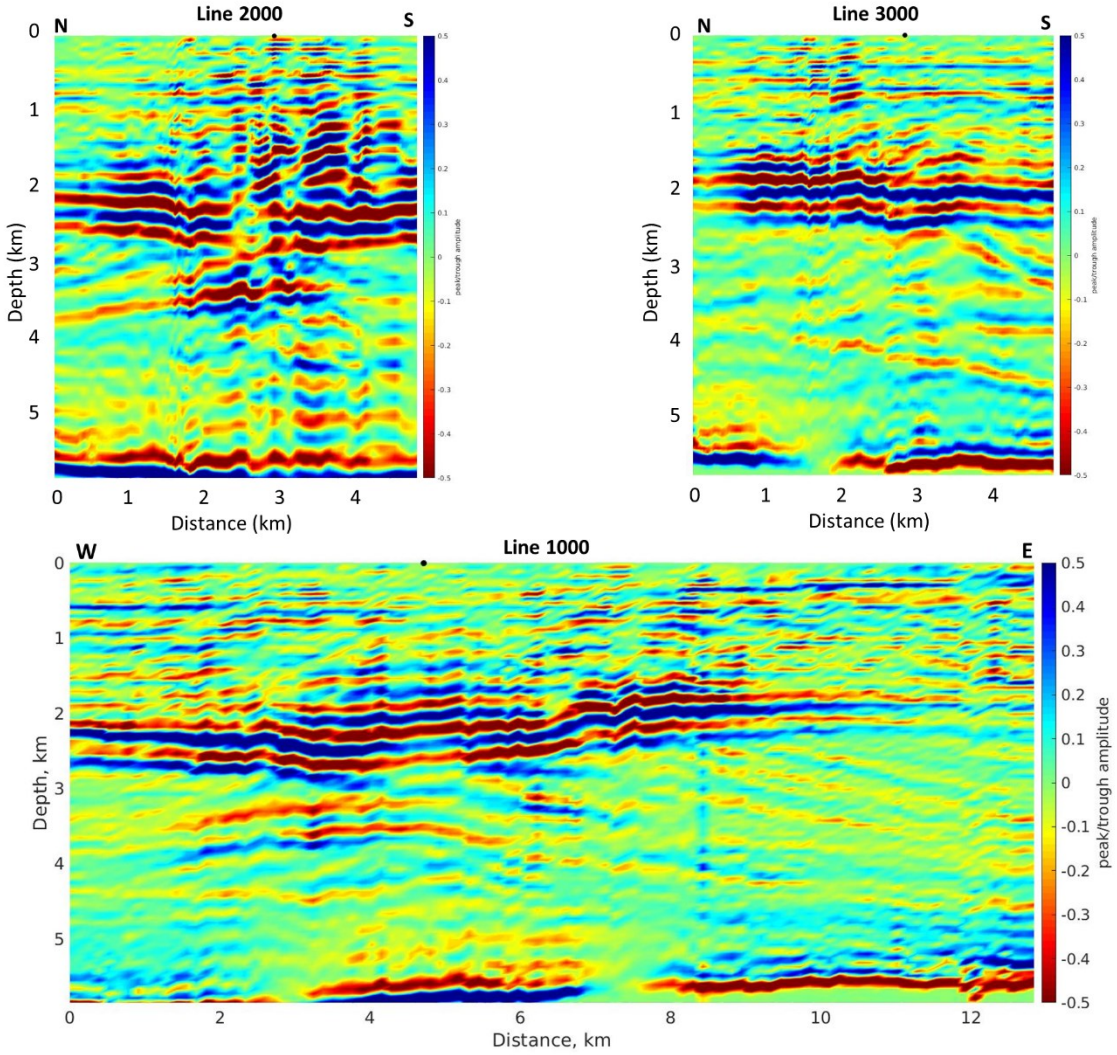

Fig. 2.6: *Depth-migrated images of Event 1 over all three lines. These images were produced using an event depth of 5.85 km, versus the catalog depth of 5.24 km. See Fig. 2.7b for a depth-migrated image of Event 1, Line 1000 processed with a 5.24 hypocenter depth.*

is at the maximum time. Fig. 2.5 illustrates the processing steps starting with pre-processed filtered data (2.5a), flipped data (2.5b), and depth-migrated data (2.5c) for Event 1, Line 1000. Sp conversions nearest the surface are waveforms close to the S-wave, and deeper Sp conversions are waveforms close to the source and therefore the P-wave arrival (Bath &

Stefánsson, 1966). To interpolate for depth, we resample time and depth at the delta t time increment, (one over the sampling rate of the instrument (1/250sps = 0.004 seconds)), using the time difference between direct S-wave travel times and S-to-P travel times from each sampled depth from the velocity model, and depth sampling points (Baysal et al., 1983; Kirk, 1984). Travel time curves are shown for Event 5 in Fig. 2.4. Final depth-migrated images for Event 1, Lines 1000, 2000, and 3000 are shown in Fig. 2.6.

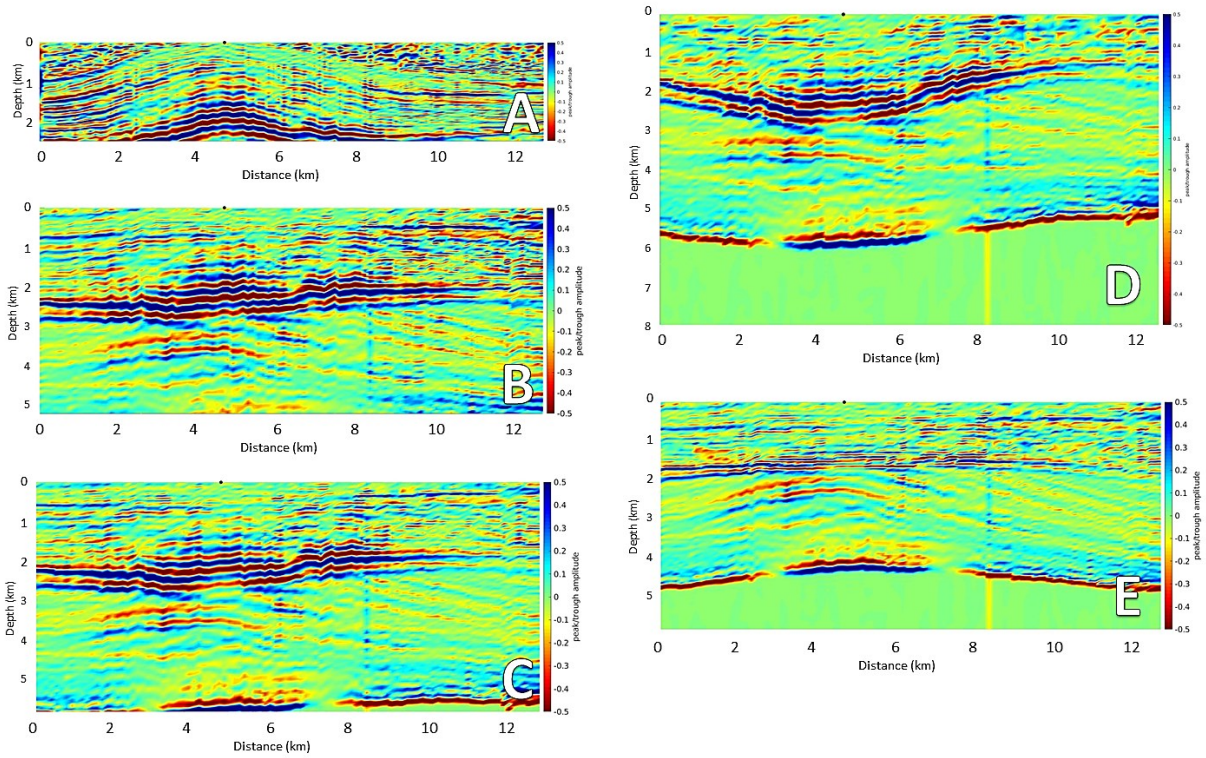

Fig. 2.7: *Testing the correctness of the catalog depth and velocity model. All images are from Event 5, Line 1000 (A) 2.5 km source depth (B) 5.24 km source depth (C) 5.85 km source depth (D) 8.0 km source depth (E) Velocity model altered to include a LV layer at 1.0-1.5 km and 3.9-4.1 km; processed with 5.85 km source depth. Plots A-E are west-to-east from left-to-right.*

Synthetic seismograms were created using frequency-wavenumber integration to test the imaging technique. The synthetics were produced for a hypothetical strike-slip event at 4.5 km depth for 20 stations in a 4 km long array with 200-meter receiver spacing. This method uses a gradient velocity model of a vertically inhomogeneous half-space to produce smooth turning rays, and the Brune earthquake fault-source model for the strike-slip source (Brune, 1970). The integration is over the real axis of the wavenumber with the adaptive Filon's integration method, which requires the Green's function for moment computations, and an integral kernel that is the product of the vertical wave function and the Bessel function (Barker, 1984; Langston, 1987). If the velocity model and catalog depth are both correct, the P-wave arrival will be located exactly at the source depth. To test our velocity model and source depths, events with an apparent "cut" P-wave arrival were identified and reprocessed at deeper and shallower depths to observe the effect on the images. Event 1 appeared to be missing the P-wave arrival at the catalog depth of 5.24 km (Fig. 2.7b). This event was completely reprocessed using an event depth of 2.5 km (Fig. 2.7a), 8.0 km (Fig. 2.7d), and finally, 5.85 km (Fig. 2.7c).

The velocity model was also tested and altered to include low-velocity zones between 1-1.5 km depth, and at 4 km depth. Pre-processed event data from Event 1 and the altered model were used to conduct a depth-migration (Fig. 2.7e). The synthetic data were reprocessed to observe the effect of low velocity layers in the model (Fig. 2.8). Both tests (real and synthetic

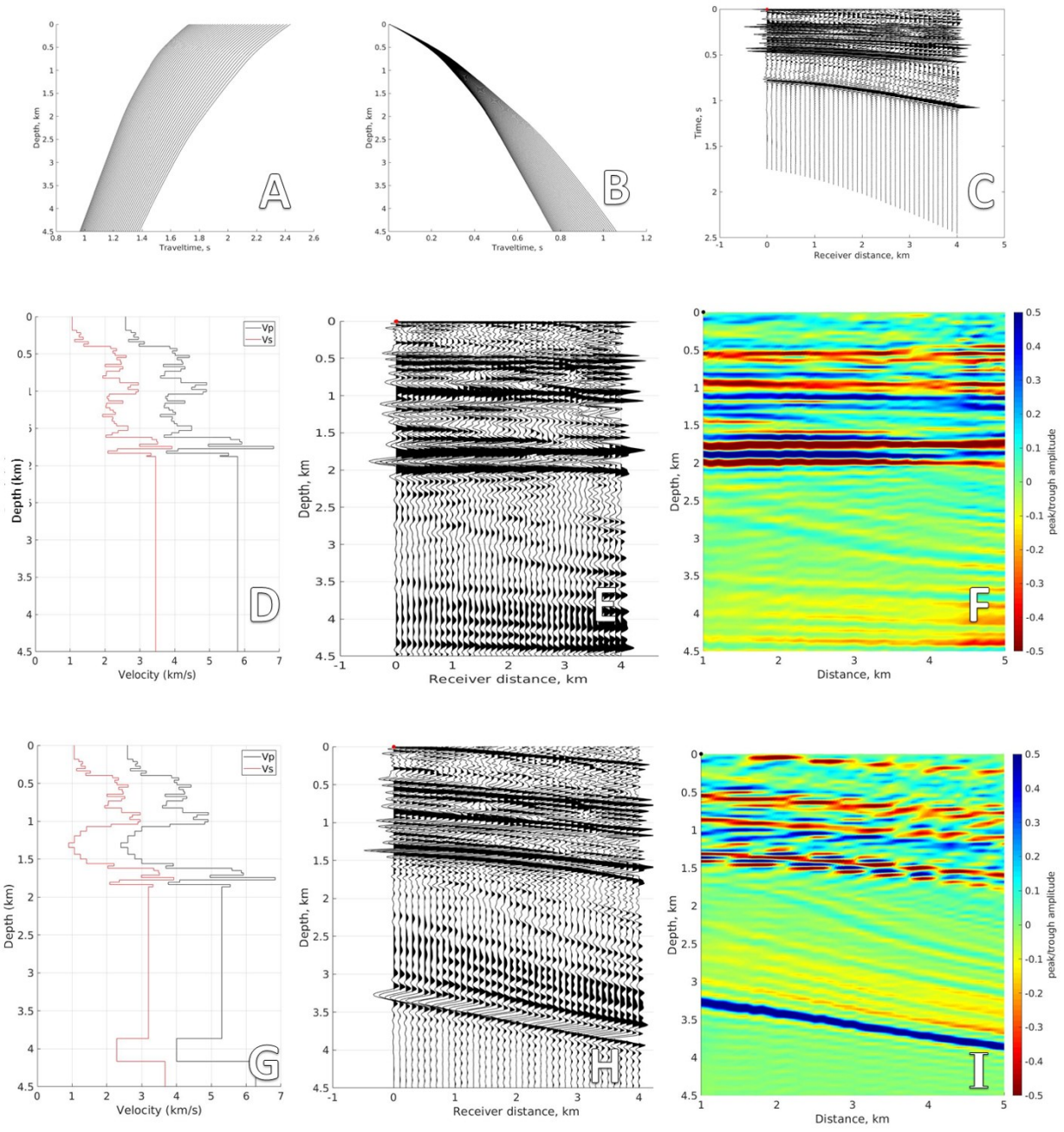

Fig. 2.8: *Synthetic seismograms. (A) S-to-P travel time versus depth curve. (B) S minus Sp travel time versus depth curve. (C) Pre-processed, filtered, and time-reversed data (D)1D velocity model (E) Depth-migrated image as it corresponds to the 1D velocity model (F) Density plot of depth-migrated data (G) Altered velocity model; LV layers at 1.0-1.5 km, and 3.9-4.1 km (H) Resulting depth-migration from altered 1D model (I) Resulting density plot from altered 1D model.*

data) had a notable effect on the dip of the stratigraphy. If the reprocessed data with velocity changes resulted in the same structure with different velocity models, then our processing methods contain an error that supersedes changes in velocity. If the reprocessed data show a change in the resulting images (in our case, from flat-lying strata to dipping strata), then the original velocity model is a better fit.

Chapter 3—Results & Discussion

Vertical Resolution

Frequencies from this study range between 5 and 20Hz over different events and station records. Frequency is used to calculate the wavelength: the quotient of velocity and frequency. When layer thicknesses are greater than ¼ of the wavelength (λ), we are able to distinguish full

Table 3: Vertical Resolution Events—Three Arrays

λ = Vp/f	Line 1000	Line 2000	Line 3000
	λ/4 (meters)	**λ/4 (meters)**	**λ/4 (meters)**
Event 1	145	72.5	181.3
Event 2	145	290	290
Event 3	290	290	290
Event 4	145	72.5	145
Event 5	96.6	96.6	145

layers. Vertical resolution is generally described as λ/4 for this reason. Using our observed frequencies, we are able to resolve layers with thicknesses of greater than 290m (5Hz data) and 75.2m (20Hz data), though at least three events (1, 4, and 5) have clear bimodal distributions with a second peak at 35-40 Hz. This higher frequency content may increase the resolving power.

Polarity Reversals

There are polarity reversals evident in at least one seismic line of all events except event 2. In reflection surveys, reversals can be caused by a change in acoustic impedance (Onajite, 2013), and can also be a record of the earthquake source radiation pattern (Lowrie, 2007). When sand has a higher acoustic impedance than overlying shale, the sand is interpreted to be water-saturated. Hydrocarbons will have an even lower acoustic impedance than shale (Onajite, 2014).

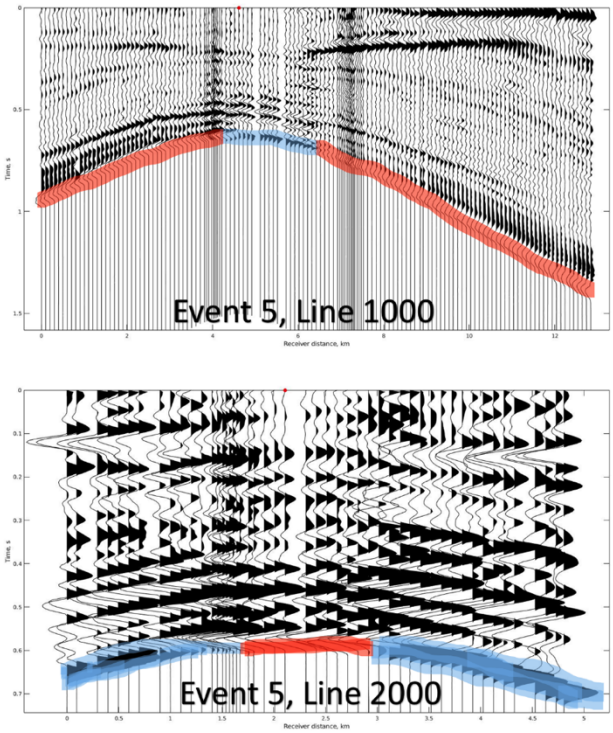

***Fig. 3.1**: P-wave polarity reversal in Event 5, Line 1000 & 2000. Time series data are pre-processed. Blue and red highlights indicate positive and negative amplitudes, respectively.*

In this region of Oklahoma, it would not be exceptional to see evidence of hydrocarbons in reflection data (Boyd, 2008; Boyd, 2002). In our passive array experiment, P-waves travel from

the source to the receiver and pass through each layer one time (Fig. 1.1.2). No P-wave reflections are occurring. Due to this fact, P-wave polarity changes across the array are an effect of earthquake source radiation patterns. Event 5 exhibits a polarity reversal on Line 1000 and Line 2000 as shown in Fig. 3.1. We also see polarity reversals across Line 1000 in Event 1. Fig. 2.7e shows a low-high-low polarity change from west-to-east across the P-wave arrival. The reversals appear to extend upward and give the appearance of "steps" in the image. This is especially evident in Fig. 2.7. The reversal occurs near a horizontal distance of 3 kilometers, and the "steps" appear at the same distance. This is true for the opposite side of the array. We see more "steps" at a horizontal distance of 7 kilometers. Polarity changes in the data could be used to map P-wave radiation and first motions.

Sp Conversion in N-S and W-E Profiles

The concept of wave phase conversion allows identification of discontinuities in the crust, and correlation of arrival times from discontinuities to a known velocity model, which can be used to interpolate the boundaries from time to depth (Bath & Stefánsson, 1966; Bock, 1984; Smith, 1970; Stein & Wysession, 2009). Each waveform in the recorded data between the P-arrival and S-arrival is hypothesized to be an Sp conversion. After the data are corrected and time

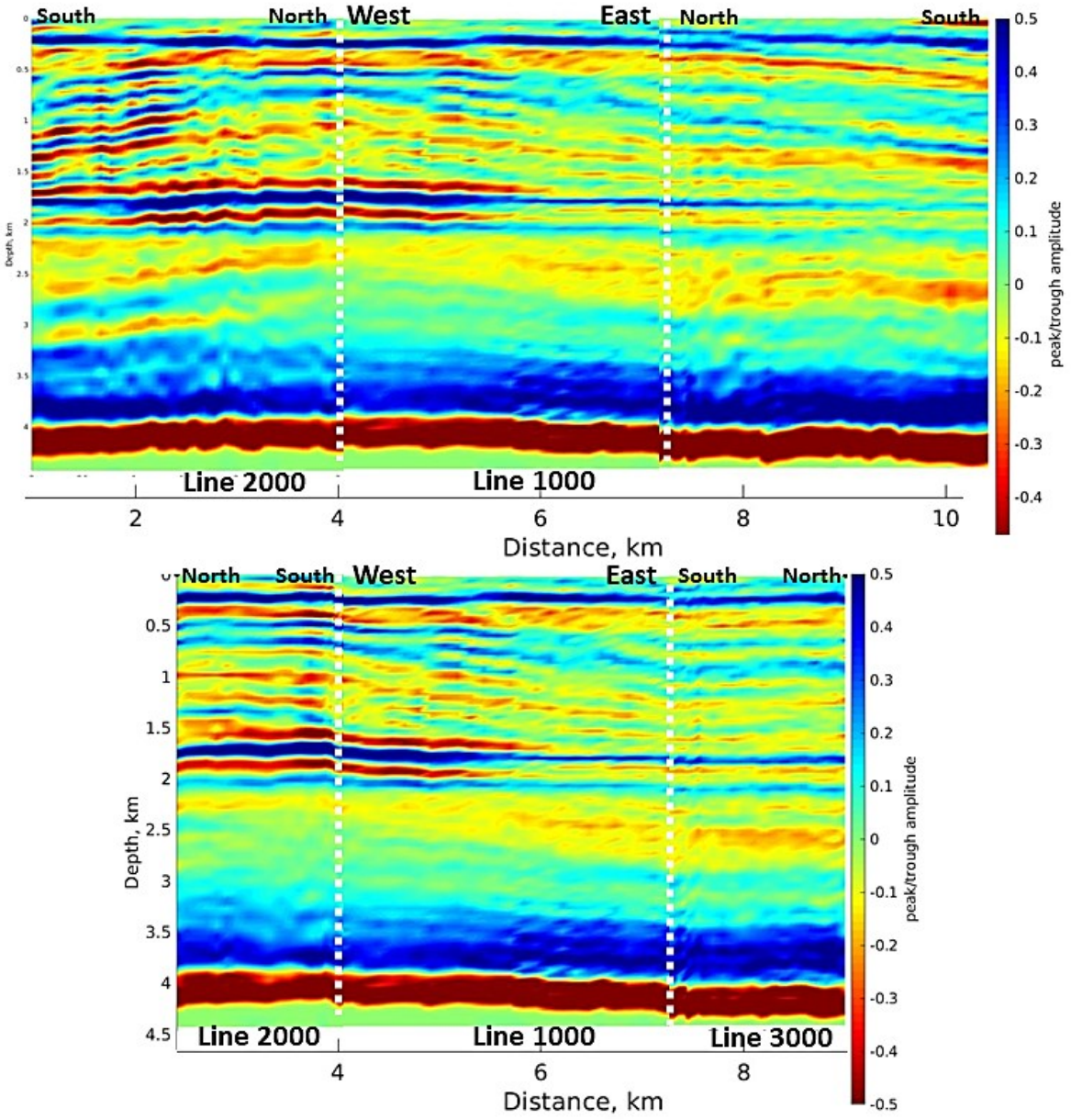

Fig. 3.2: *Cut and linked depth-migrated images from Event 2, Lines 1000, 2000, and 3000. White dotted line indicates the joining point of each profile.*

converted to depth, the waveforms can be used to indicate discontinuities at depth. Events with larger magnitudes have recordings with a waveform amplitude many times greater than the recorded noise. This high signal-to-noise ratio is ideal. For these reasons, the recordings with the most robust signal-to-noise ratio are from events 1 and 5. Event 2 also has a high signal-to-noise ratio. The local magnitude (ml) of events 1 and 5 are 2.28 and 2.95, respectively. Event 3 has a very low signal-to-noise ratio, resulting from the low magnitude of ml 0.78, but has a desirable epicenter location and median depth (Sawi & DeShon, 2016). Depth-migrated and colored density images for each event and each of the three arrays are illustrated in the supplementary figures in Appendix B. Aligned sets of peaks and troughs indicating positive and negative velocity contrasts, respectively, are consistent and evident in the data sets across the arrays. In all 5 events, we observe large S-waves and many large Sp conversions that dominate the P-wave coda. This could be indicative of a strike-slip source, as shear waves tend to dominate the signal in these types of earthquakes (Takemura et al., 2016). The north and east components demonstrate large S-wave arrivals (Fig. 1.1.1).

Event 1 is the deepest at 5.24 kilometer catalog depth, has a local magnitude of 2.28, and produces the most complete images of the stratigraphy out of all events (Fig. 2.5, 2.6). This earthquake is located south-southeast of the intersection of Line 1000 and Line 2000 (Fig. 2.1). Array 1000 runs from west to east over horizontal distance 0 to 13 km. Event 1, line 1000 (Fig. 2.6) shows two clear discontinuities at 2.0 and 2.5 kilometers depth near the center of the array and appear to dip slightly to the west largely due to polarity reversals. Event 2, located to the northwest of the three array lines (Fig. 2.1) with a depth of 4.43 km and ml 2.79, displays flat lying strata and no polarity reversals in any of the three arrays. There are clear discontinuities at

0.5 km depth, and near 1.5 and 2.0 km (Fig. 3.2). The P-wave of Event 2 is not at exactly 4.43 kilometers which means that the depth could be incorrect. If Event 2 depth was reprocessed to ~4.25 km, the P-wave arrival may be in the correct spot, though the strata would be migrated.

Adjustment of the depth in event 1 (Fig. 2.7) illustrates the effects of source depth errors. When an error exists, the P-wave arrival will not appear exactly at the calculated source depth. If the source depth is much too deep (2.7d), strata will appear to be dipping towards the epicenter location. If the source depth is much too shallow, we see the opposite effect; strata will appear to sip away from the epicenter location (2.7a). The velocity model can also be adjusted and we see similar responses. When low velocities are input into the depth-migration, the modeled strata dips away from the epicenter (2.7e). The P-wave arrival also migrates to shallower depths. A velocity model with high velocity zones produces a similar response to the deep depth test: we see strata dipping towards the epicenter (Fig.2.7d).

Event 3 is located to the far southeast of the array, and has a depth of 3.94 km, and an ml of 0.78. This event is relatively low magnitude, but shows obvious discontinuities at 0.5 km, 2.0 to 2.2, and 3.5 kilometers depth (Fig. A3). Peaks and troughs in this event's images are more evident to the south and eastern sections of arrays 2000/3000 and 1000, respectively, due to the southeastern epicenter (Fig. 2.1). Event 4, which has a hypocenter at 3.32 km depth and ml 2.02, is located south of the southernmost receiver of the array (Fig. 2.1). Clear discontinuities are located at depths of 0.5, 2.0, 2.3, and 3.2 km, which is relatively consistent

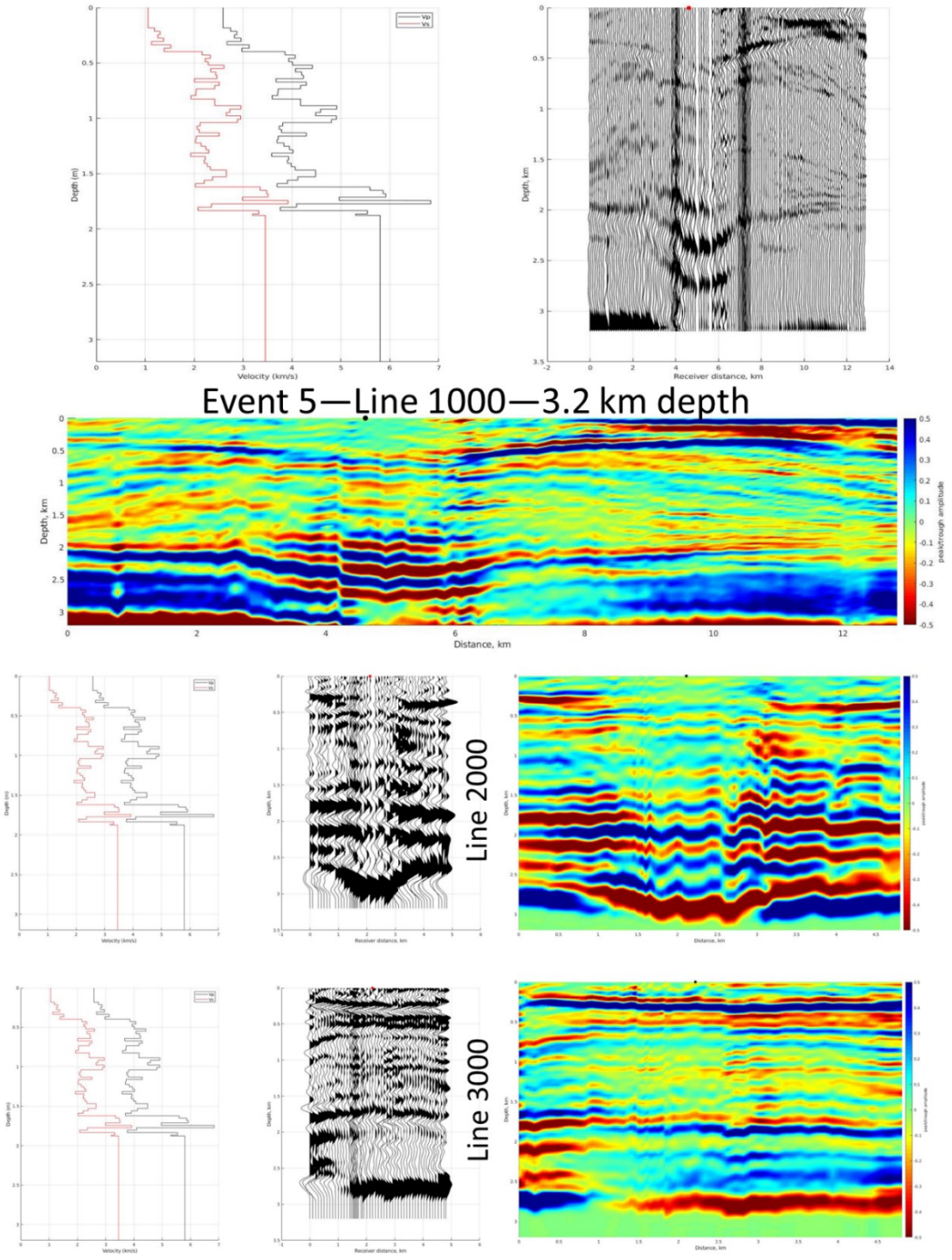

Fig. 3.3: *Event 5, Lines 1000, 2000, and 3000. Depth adjusted to 3.2 kilometers. Original depth images available in Appendix B, supplementary figures.*

with the depths of discontinuities in the previous three events (Fig. A4). Event 5 is located in proximity to the cross-hairs of Lines 1000 and 2000 (Fig. 2.1) with a depth of 2.96 km and a local magnitude of 2.95. Discontinuities are visible at depths of 0.5, 2.0, and 2.3 km (Fig. A5). Original images of Event 5 decapitated the P-wave arrival. Depths were then adjusted to 3.2 km to produce new images with the full waveforms intact (Fig. 3.3).

Each event recorded along line 1000 exhibits strong, lateral discontinuities at 0.5 kilometers depth (Fig. 2.7, 3.2, 3.3). Lines 2000 and 3000 show discontinuities of similar intensity at depths of 0.5 kilometers. The 0.5 km discontinuity is relatively flat with no clear dip direction. Along line 1000, two to three discontinuities exist between 2- and 3-kilometers depth.

Synthetic Seismograms

The P-waves from the hypothetical strike-slip event in the synthetic seismograms should arrive exactly at the 4.5 km depth line, but they do not. We investigate the effect of depth manipulation on the synthetic seismograms to confirm that this is true. Fig. 3.4 shows the effect of a higher (5.5 km) and lower (3.5 km) input depth when completing the time-depth migration. A depth greater than the original synthetic depth (5.5 km vs 4.5 km) results in a strata dipping towards the epicenter and will migrate apparent discontinuities to deeper depths in the west and shallower depths in the east (Fig. 3.4). Using a shallower depth (3.5 km) than the original synthetic depth of 4.5 km results in strata that appears to dip away from the epicenter. When we tested the synthetic seismograms for errors in the velocity model. We introduced two low velocity layers and the strata responded by migrating the P-wave arrival to shallower depths

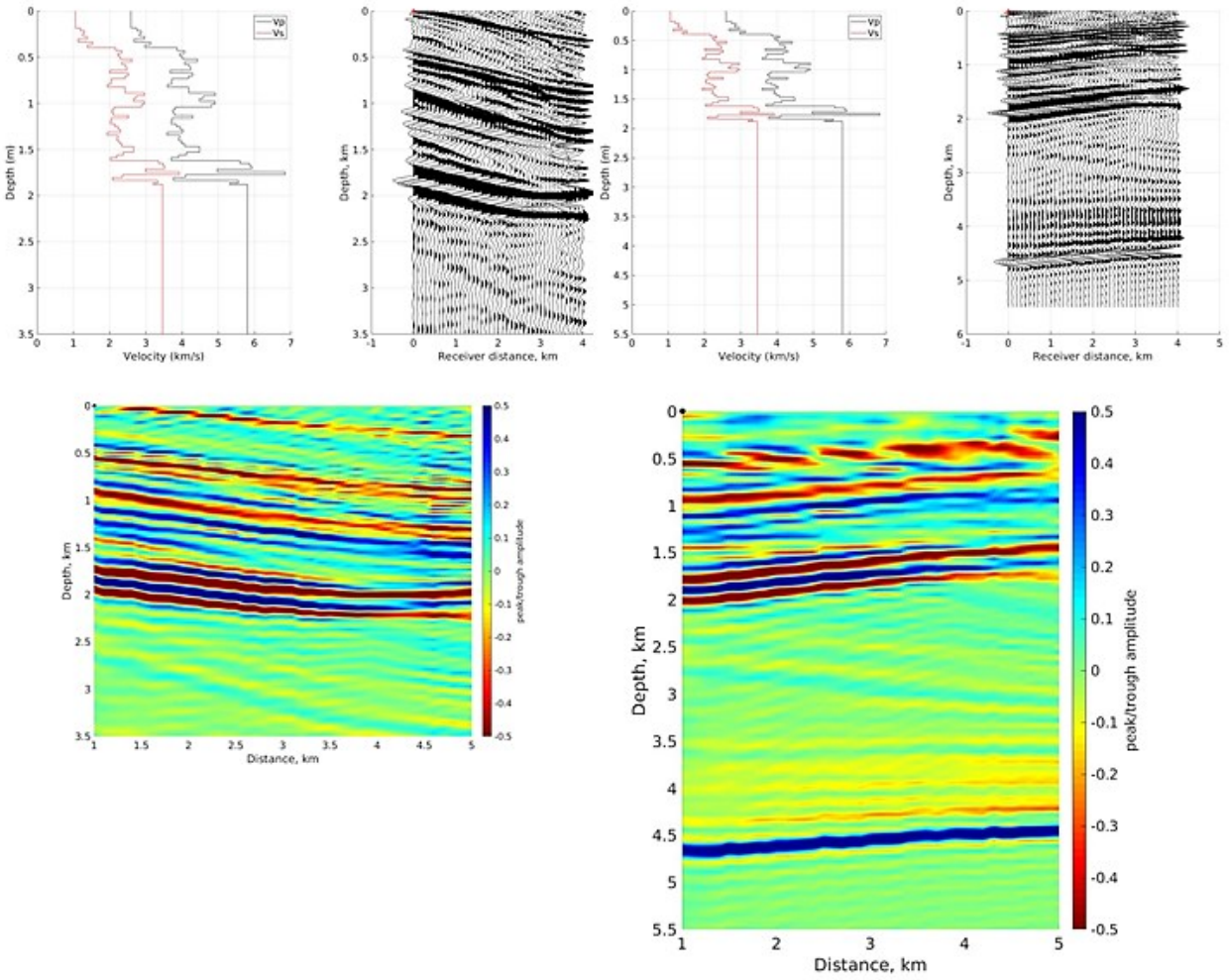

Fig. 3.4: *Synthetic seismogram plots for a source depth of 3.5 km (left) and 5.5 km (right). Original synthetic depth is 4.5 km (see Fig. 2.8).*

and strata appear to be dipping away from the epicenter (Fig. 2.8). The low-velocity layer test and depth test with a shallower input show similar effects on the modeled Sp conversion depths (Fig. 2.8; Fig.3.4).

Correlating Discontinuities in Time and Depth

We anticipated largely flat lying Paleozoic sediments in our study area that increase in thickness to the south and towards the central part of the state (west), with no major active fault zones affecting the stratigraphy (Hoffman et al., 1989; Johnson, 2008; Marsh and Holland, 2016). Discontinuities observed in all five events correspond closely with velocity boundaries in the 1D velocity model, and can be correlated with the stratigraphic columns in Fig. 1.3 that extend to a depth of 1.86 kilometers (Gianoutsos et al., 2014). The first major discontinuity that is consistent across events and seismic lines occurs at 0.5 kilometers depth and corresponds to the base of the Permian redbed sandstones and shales and the top of the Pennsylvanian limestones, sandstones, and shales (Fig. 1.1.1; Fig. 1.2; Johnson, 2008). This same discontinuity is consistent with the lithology and depth data from oil and gas well data in Grant County as shown in Fig. 1.3, and with geologic interpretations shown in the cross section of Fig. 1.2 (Johnson, 2008).

The depth to the basement in north-central Oklahoma is anywhere from 1.6-2.4 km according to publicly available OK well data (Campbell, J.A., 2003). The depth to the basement nearest the array location (west of the Nemaha Uplift) is ~2.1 km, as shown in Fig. 1.2 (Johnson, 2008). Processed images from each of the five events across all three seismic lines display discontinuities near 2 km depth (Fig. 2.6, 2.7, 2.8, 3.2, 3.3, 3.5). The synthetic data shown in Fig. 2.8 argues the same point. The stratigraphy column interpreted from well data in Grant County (Fig. 1.3) ends at a maximum depth of 1.86 km with sandstone as the base lithology, pointing to the fact that pre-Cambrian crystalline basement rock is at a deeper depth.

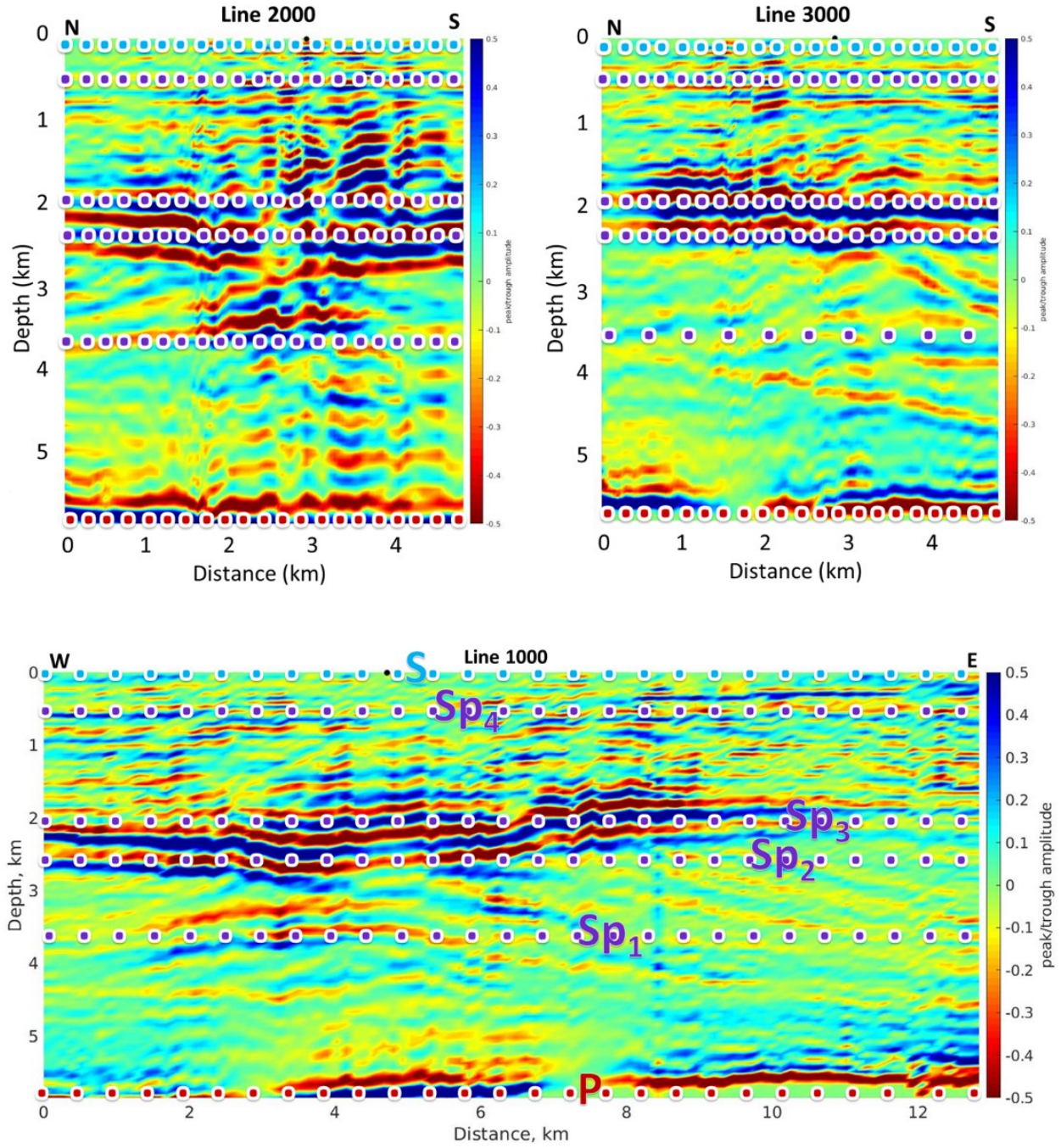

Fig.. 3.5: *Event 1 depth-migrated density images. P, S, Sp1,2,3,4 arrivals from Fig. 1.1.1 are identified in the images for all three array lines. Phases are labeled on the sub-figure for Line 1000.*

The sonic log used to create a velocity-depth model also ends at a depth of 1.87 km. By combining the stratigraphy column, average regional well depths, sonic log data, and our processed and corrected Sp conversion images, we can interpret the discontinuities near 2.0 kilometers to be the top of the basement.

Of the original 270 seismic events, 265 occurred at 2.5 km depth or deeper (Sawi & DeShon, 2016; Table 4), which indicates that the faults that are being activated and causing seismic events are within the crystalline basement rock (Sawi & DeShon, 2016; Ellsworth, 2013; McGarr et al., 2002). The maximum depth of fracking and extraction/injection wells resides within the stratigraphy of the sedimentary rocks, and fracturing these rocks can change the mass and volume of a load which changes the normal stress and shear stress and is enough to activate a fault (Ellsworth, 2013; McGarr et al., 2002).

One notable problem with adjusting the event depths to produce images with appropriate source depths is that the problem could hypothetically be resolved by adjusting the velocity model as well. Through testing the effects of shallow and deep source depths as well as high and low velocity layers, we found that deep source depths and high velocity layers change the depth-migration image in the same way; both produce epicenter-dipping strata. The shallow source depths and low velocity layers create strata dipping away from the epicenter (Fig. 2.7). This means that we could potentially solve our P-wave decapitation issue by either increasing the source depth or adding high velocity layers in the velocity model. This simple relation is complicated by the fact that the low velocity layer test resulted in a P-wave migration from about 6km depth up to 5.5km depth. This makes solution by velocity model updates more complicated.

Table 4: Number of Events by Depth—Data from Sawi & DeShon, 2016

Depth from Surface (km)	**Depth from Surface (feet)**	**Number of Events**
0.0 - 0.49	0 - 1640	0
0.5 - 0.99	1640 - 3280	1
1.0 - 1.49	3280 - 4921	1
1.5 - 1.99	4921 - 6561	2
2.0 - 2.49	6561 - 8202	1
2.5 - 2.99	8202 - 9842	22
3.0 - 3.49	9842 - 11483	43
3.5-3.99	11483 - 13123	31
4.0-4.49	13123 - 14763	23
4.5-4.99	14763 - 16404	36
5.0-5.49	16404 - 18044	56
5.5-5.99	18044 - 19685	26
6.0-6.49	19685 - 21325	12
6.5-6.99	21325 - 22966	8
7.0-7.49	22966 - 24606	8
7.5 +	24606 +	0

We see many reflectors in the depth-migrated images that appear to be steeply dipping. These phases are P-wave reverberations in the structure. The synthetic data (Fig. 2.8f) displays flat-lying strata with some dipping seismic phases beginning at 2 km depth. These reflectors are weak, but are also present in Event 5 (Fig. 3.5) between Sp_1 and Sp_2, and just below Sp_1. Event 5, Line 1000 has P-wave reverberations in the data on the western and eastern extents of the array between depths of 0.5 and 2.0 km. Ps phases and P-wave reverberations are very small in our data. We do not have much of a P-wave response in the pre-processed seismic data (Fig. 1.1.1) because P waves are generally small due to the radiation pattern of strike-slip earthquakes.

Chapter 4—Conclusions

Conclusions

Sp conversions produced by local events in regional arrays can be used to identify or confirm structural discontinuities in the crust. Through detailed source modeling, we are able to study local seismic sources more effectively, observe how predicted stratigraphy affects waveforms, and how source hypocenter depth and location impacts produced waveforms. By modeling the phases and the velocity structure we confirmed Sp conversion times and depths using travel times, amplitude, other phases, stratigraphy, and well data. Two major Sp conversions associated with large discontinuities in velocity structure were identified around 0.5 kilometers and ~2.1 kilometers depth. Images produced from each of the 5 events along all three seismic lines were relatively consistent. The discontinuity at 0.5 km is confirmed to be the boundary between the Permian redbed sandstones/shales and the Pennsylvanian limestones, sandstones, and shales. The ~2.1 km discontinuity was less conformable across all lengths of the arrays, but still evident in each image and interpreted to be the boundary between the Cambrian limestone/dolomite and the pre-Cambrian crystalline basement.

Vertical resolution in this study at one quarter the wavelength ($\lambda/4$) ranges from 290 meters to 72.4 meters. We are able to resolve layers of thicknesses greater than this. We are also able to identify layer boundaries at resolutions of $\lambda/32$. Our best and worst resolutions using this definition are 9 meters and 37 meters ((Rafaelsen, 2012). Our horizontal resolution ranges from 1km to 8 km. The final images and resolution calculations demonstrate that passive arrays

installed at dense receiver spacing can reliably image crustal stratigraphy in the absence of active-sources.

REFERENCES

Anderson, K.R., Sweet, J.R., Woodward, R., (2016). IRIS Community Wavefield Experiment in Oklahoma. Incorporated Research Institutions for Seismology. Dataset/Seismic Network. 10.7914/SN/YW_2016. https://doi.org/10.7914/SN/YW_2016.

ANSS catalog, United States Geological Survey, http://earthquake.usgs.gov/earthquakes/search/, accessed April 2018.

Bath, M. and Stefánsson, R., (1966). SP conversion at the base of the crust. Annals of Geophysics, 19(2), pp.119-130.

Barker, J.S., 1986. A SEISMOLOGICAL ANALYSIS OF THE MAY 1980 MAMMOTH LAKES, CALIFORNIA, EARTHQUAKES.

Baysal, E., Kosloff, D.D. and Sherwood, J.W., (1983). Reverse time migration. Geophysics, 48(11), pp.1514-1524.

Bock, G. and Ha, J., (1984). Short-period SP conversion in the mantle at a depth near 700 km. Geophysical Journal International, 77(2), pp.593-615.

Bortfeld, R., (1989). Geometrical ray theory: Rays and traveltimes in seismic systems (second-order approximations of the traveltimes). Geophysics, 54(3), pp.342-349.

Boyd, D.T., (2008). Stratigraphic Guide to Oklahoma Oil and Gas Reserviors. Oklahoma Geological Survey, University of Oklahoma.

Boyd, D.T., (2002). Map of Oklahoma Oil and Gas Fields. Okahoma Geologicial Survey GM36.

Brocher, T.M., (2005). Empirical relations between elastic wavespeeds and density in the Earth's crust. Bulletin of the seismological Society of America, 95(6), pp.2081-2092.

Brune, J.N., (1970). Tectonic stress and the spectra of seismic shear waves from earthquakes. Journal of Geophysical Research 75, 4997–5009.

Campbell, J.A., (2003). Wells drilled to basement in Oklahoma.

Chen, X., Nakata, N., Pennington, C., Haffener, J., Chang, J.C., He, X., Zhan, Z., Ni, S. and Walter, J.I., (2017). The Pawnee earthquake as a result of the interplay among injection, faults and foreshocks. Scientific Reports, 7(1), p.4945.

Crain, E., (1984). Crain’s Petrophysical Handbook, Online Shareware Petrophysics Training and Reference Manual. Available on:< http://www. spec2000. net/01-index. htm>. Access on: April 2018.

Darold, A.P., Holland, A.A., Morris, J.K. and Gibson, A.R., (2015). Oklahoma earthquake summary report 2014. Oklahoma Geol. Surv. Open-File Rept. OF1-2015

De Hoop, A.T., (1960). A modification of Cagniard's method for solving seismic pulse problems. Applied Scientific Research, Section B, 8(1), pp.349-356.

Ellsworth, W.L., (2013). Injection-induced earthquakes. Science, 341(6142), p.1225942.

Gianoutsos, N.J., Kruger, J.D, Nelson, P.H., and Higley., D.K. (2014). Lithology of Paleozoic rock units in 62 wells, Anadarko Basin, Oklahoma, chap. 10, in Higley, D.K., compiler, Petroleum systems and assessment of undiscovered oil and gas in the Anadarko Basin Province, Colorado, Kansas, Oklahoma, and Texas—USGS Province 58: U.S. Geological Survey Digital Data Series 69–EE, 6 p. http://dx.doi.org/10.3133/ds69EE.

Hai-Ming, Z. and Xiao-Fei, C., (2001). Self-adaptive Filon's integration method and its application to computing synthetic seismograms. Chinese Physics Letters, 18(3), p.313.

Hincks, T., Aspinall, W., Cooke, R. and Gernon, T., (2018). Oklahoma's induced seismicity strongly linked to wastewater injection depth. Science, 359(6381), pp.1251-1255.

Hoffman, P.F., Bally, A.W. and Palmer, A.R., (1989). Precambrian geology and tectonic history of North America. The geology of North America—an overview, pp. 447-512.

Holland, A.A., (2013). Earthquakes triggered by hydraulic fracturing in south-central Oklahoma. Bulletin of the Seismological Society of America, 103(3), pp.1784-1792.

IRIS, (2018). IRIS earthquake browser, Incorporated Research Institutions for Seismology, http://ds.iris.edu/ieb/, (accessed November 2018).

Johnson, K.S., (2008). Geologic history of Oklahoma. Earth sciences and mineral resources of Oklahoma: Oklahoma Geological Survey Educational Publication, 9, pp.3-5.

Johnson, K.S., Hinshaw, G.C. and Northcutt, R.A., (2000). Petroleum production from platform carbonates of Oklahoma. In Platform carbonates in the southern mid-continent, 1996 symposium: Oklahoma Geological Survey Circular (Vol. 101, pp. 1-11).

Keranen, K.M., Weingarten, M., Abers, G.A., Bekins, B.A. and Ge, S., (2014). Sharp increase in central Oklahoma seismicity since 2008 induced by massive wastewater injection. Science, 345(6195), pp.448-451.

Kirk, S., (1985). Borehole compensated sonic 26N-7W-15, Mobil Oil Corporation, pp.1-32.

Langston, C.A., (1987). Depth of faulting during the 1968 Meckering, Australia, earthquake sequence determined from waveform analysis of local seismograms. Journal of Geophysical Research: Solid Earth, 92(B11), pp.11561-11574.

Langston, C.A., (1979). Structure under Mount Rainier, Washington, inferred from teleseismic body waves. Journal of Geophysical Research: Solid Earth, 84(B9), pp.4749-4762.

Li, Z., Peng, Z., Hollis, D., Zhu, L. & McClellan, J., (2018). High-resolution seismic event detection using local similarity for large-N arrays, Sci. Rep., 8(1), 1646, doi:10.1038/s41598-018-19728-w.

Lowrie, W., (2007). Fundamentals of geophysics. Cambridge university press.

Marsh, S. and Holland, A., (2016). Comprehensive fault database and interpretive fault map of Oklahoma. Oklahoma Geol. Surv. Open-File Rept., p.15.

McGarr, A., Simpson, D., Seeber, L. and Lee, W., (2002). Case histories of induced and triggered seismicity. International Geophysics Series, 81(A), pp.647-664.

McNamara, D.E., Rubinstein, J.L., Myers, E., Smoczyk, G., Benz, H.M., Williams, R.A., Hayes, G., Wilson, D., Herrmann, R., McMahon, N.D. and Aster, R.C., (2015). Efforts to monitor and characterize the recent increasing seismicity in central Oklahoma. The Leading Edge, 34(6), pp.628-639.

Nakata, N., Oklahoma velocity model, via personal correspondence, March 2018.

Onajite, E., (2013). Seismic data analysis techniques in hydrocarbon exploration. Elsevier.

Perry, W.J., (1989). Tectonic evolution of the Anadarko Basin region, Oklahoma (No. 1866). Department of the Interior, US Geological Survey.

Rafaelsen, B., (2006). Seismic resolution and frequency filtering. Univ. Tromso Lecture Series, Tromso, Norway.

Sawi, T., DeShon, H.R., (2016). IRIS community wavefield experiment earthquake catalog—local events. Southern Methodist University.

Sheriff, R.E., (2002). Encyclopedic dictionary of applied geophysics. Society of exploration geophysicists.

Smith, W.D., (1970). S to P conversion as an aid to crustal studies. Geophysical Journal International, 19(5), pp.513-519.

Stein, S. and Wysession, M., (2009). An introduction to seismology, earthquakes, and earth structure. John Wiley & Sons.

Sweet, J.R., Anderson, K.R., Bilek, S., Brudzinski, M., Chen, X., DeShon, H., Hayward, C., Karplus, M., Keranen, K., Langston, C. and Lin, F.C., (2018). A community experiment to record the full seismic wavefield in Oklahoma. Seismological Research Letters, 89(5), pp.1923-1930.
Wood, R.H., 1913. Contributions to economic geology, 1911, Part II, Mineral fuels--Oil and gas development in north-central Oklahoma (No. 531-B).

Takemura, S., Kobayashi, M. and Yoshimoto, K., (2016). Prediction of maximum P-and S-wave amplitude distributions incorporating frequency-and distance-dependent characteristics of the observed apparent radiation patterns. Earth, Planets and Space, 68(1), p.166.

APPENDIX A: SUPPLEMENTARY TABLES

Table A1: Kirk 1985 Sonic Log Velocity Model

Depth, km	Vp, km/s (transit time)	Density (ρ), g/cm3 (Brocher, 2005)	Vs km/s (Brocher, 2005)	Thickness, km
0.00000	2.59000	1.05807	2.12027	0.18300
0.18300	2.74595	1.19051	2.16321	0.03036
0.21336	2.87547	1.30297	2.19545	0.03048
0.24384	2.82222	1.25652	2.18254	0.03048
0.27432	2.95922	1.37652	2.21481	0.03048
0.30480	2.67368	1.12867	2.14391	0.03048
0.33528	3.12615	1.52430	2.25037	0.03048
0.36576	2.97366	1.38924	2.21804	0.03048
0.39624	3.85823	2.16396	2.37320	0.03048
0.42672	4.06400	2.33401	2.40226	0.03048
0.45720	3.93290	2.22639	2.38389	0.03048
0.48768	4.01053	2.29043	2.39482	0.03048
0.51816	4.41739	2.60974	2.45079	0.03048
0.54864	4.06943	2.33841	2.40302	0.03048
0.57912	4.19835	2.44144	2.42078	0.03048
0.60960	4.23333	2.46891	2.42557	0.03048
0.64008	3.67229	2.00545	2.34560	0.03048
0.67056	4.29296	2.51522	2.43373	0.03048
0.70104	4.17534	2.42327	2.41762	0.03048
0.73152	3.71707	2.04399	2.35240	0.03048
0.76200	3.70803	2.03623	2.35104	0.03048
0.79248	3.59434	1.93788	2.33349	0.03048
0.82296	4.17534	2.42327	2.41762	0.03048
0.85344	4.17534	2.42327	2.41762	0.03048
0.88392	4.91613	2.95777	2.52199	0.03048
0.91440	4.58346	2.73122	2.47382	0.03048
0.94488	4.48235	2.65791	2.45975	0.03048
0.97536	4.90821	2.95265	2.52080	0.03048
1.00584	4.80757	2.88634	2.50588	0.03048
1.03632	3.81000	2.12325	2.36619	0.03048

Table A1 (continued)				
1.06680	3.73988	2.06353	2.35582	0.03048
1.09728	3.78634	2.10316	2.36272	0.03048
1.12776	4.29296	2.51522	2.43373	0.03048
1.15824	3.71707	2.04399	2.35240	0.03048
1.18872	3.69455	2.02463	2.34900	0.03048
1.21920	3.83396	2.14352	2.36969	0.03048
1.24968	3.94819	2.23907	2.38605	0.03048
1.28016	4.02111	2.29909	2.39630	0.03048
1.31064	3.58588	1.93052	2.33215	0.03048
1.34112	3.93290	2.22639	2.38389	0.03048
1.37160	3.90769	2.20540	2.38030	0.03048
1.40208	3.98431	2.26891	2.39114	0.03048
1.43256	4.06400	2.33401	2.40226	0.03048
1.46304	4.48235	2.65791	2.45975	0.03048
1.49352	4.48235	2.65791	2.45975	0.03048
1.52400	4.11892	2.37829	2.40986	0.03048
1.55448	3.90769	2.20540	2.38030	0.03048
1.58496	3.69455	2.02463	2.34900	0.03048
1.61544	5.59266	3.35024	2.63507	0.03048
1.64592	5.86154	3.48415	2.68764	0.03048
1.67640	5.91845	3.51124	2.69940	0.03048
1.70688	4.96417	2.98861	2.52926	0.03048
1.73736	6.83408	3.92092	2.92119	0.03048
1.76784	4.09128	2.35607	2.40604	0.03048
1.79832	3.76296	2.08326	2.35926	0.03048
1.82880	5.54182	3.32368	2.62566	0.03048
1.85928	5.30087	3.19165	2.58325	0.01219
1.87147	5.80000	3.45441	2.67518	6.12853

Table A2: 1D Combined Velocity Model

Depth, km	Vp, km/s (transit time)	Density (ρ), g/cm3 (Bocher, 2005)	Vs km/s (Bocher, 2005)	Thickness, km
0.00000	2.59000	1.05807	2.12027	0.18300
0.18300	2.74595	1.19051	2.16321	0.03036
0.21336	2.87547	1.30297	2.19545	0.03048
0.24384	2.82222	1.25652	2.18254	0.03048
0.27432	2.95922	1.37652	2.21481	0.03048
0.30480	2.67368	1.12867	2.14391	0.03048
0.33528	3.12615	1.52430	2.25037	0.03048
0.36576	2.97366	1.38924	2.21804	0.03048
0.39624	3.85823	2.16396	2.37320	0.03048
0.42672	4.06400	2.33401	2.40226	0.03048
0.45720	3.93290	2.22639	2.38389	0.03048
0.48768	4.01053	2.29043	2.39482	0.03048
0.51816	4.41739	2.60974	2.45079	0.03048
0.54864	4.06943	2.33841	2.40302	0.03048
0.57912	4.19835	2.44144	2.42078	0.03048
0.60960	4.23333	2.46891	2.42557	0.03048
0.64008	3.67229	2.00545	2.34560	0.03048
0.67056	4.29296	2.51522	2.43373	0.03048
0.70104	4.17534	2.42327	2.41762	0.03048
0.73152	3.71707	2.04399	2.35240	0.03048
0.76200	3.70803	2.03623	2.35104	0.03048
0.79248	3.59434	1.93788	2.33349	0.03048
0.82296	4.17534	2.42327	2.41762	0.03048
0.85344	4.17534	2.42327	2.41762	0.03048
0.88392	4.91613	2.95777	2.52199	0.03048
0.91440	4.58346	2.73122	2.47382	0.03048
0.94488	4.48235	2.65791	2.45975	0.03048
0.97536	4.90821	2.95265	2.52080	0.03048
1.00584	4.80757	2.88634	2.50588	0.03048
1.03632	3.81000	2.12325	2.36619	0.03048
1.06680	3.73988	2.06353	2.35582	0.03048
1.09728	3.78634	2.10316	2.36272	0.03048
1.12776	4.29296	2.51522	2.43373	0.03048
1.15824	3.71707	2.04399	2.35240	0.03048
1.18872	3.69455	2.02463	2.34900	0.03048
1.21920	3.83396	2.14352	2.36969	0.03048
1.24968	3.94819	2.23907	2.38605	0.03048
1.28016	4.02111	2.29909	2.39630	0.03048

Table A2 (continued)				
1.31064	3.58588	1.93052	2.33215	0.03048
1.34112	3.93290	2.22639	2.38389	0.03048
1.37160	3.90769	2.20540	2.38030	0.03048
1.40208	3.98431	2.26891	2.39114	0.03048
1.43256	4.06400	2.33401	2.40226	0.03048
1.46304	4.48235	2.65791	2.45975	0.03048
1.49352	4.48235	2.65791	2.45975	0.03048
1.52400	4.11892	2.37829	2.40986	0.03048
1.55448	3.90769	2.20540	2.38030	0.03048
1.58496	3.69455	2.02463	2.34900	0.03048
1.61544	5.59266	3.35024	2.63507	0.03048
1.64592	5.86154	3.48415	2.68764	0.03048
1.67640	5.91845	3.51124	2.69940	0.03048
1.70688	4.96417	2.98861	2.52926	0.03048
1.73736	6.83408	3.92092	2.92119	0.03048
1.76784	4.09128	2.35607	2.40604	0.03048
1.79832	3.76296	2.08326	2.35926	0.03048
1.82880	5.54182	3.32368	2.62566	0.03048
1.85928	5.30087	3.19165	2.58325	0.01219
1.87147	5.80000	3.45441	2.67518	6.12853
8.00000	6.27000	3.67147	2.77721	13.00000
21.00000	6.41000	3.73312	2.81073	21.00000
42.00000	7.90000	4.53357	3.25578	8.00000
50.00000	8.15000	4.74285	3.34496	30.00000
80.00000	8.50000	5.10465	3.47577	5.00000

APPENDIX B: SUPPLEMENTARY FIGURES

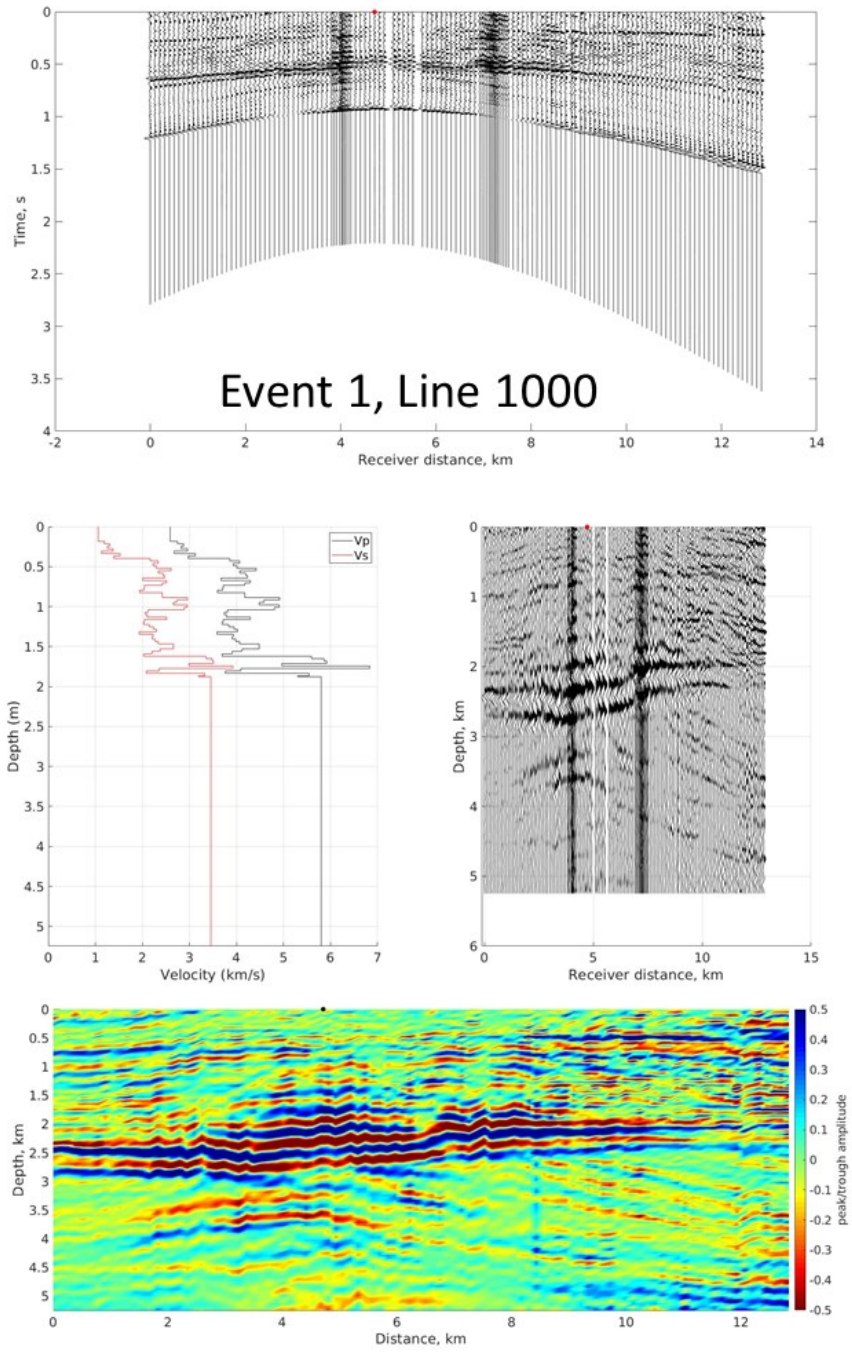

Fig. A1a: *Event 1, line 1000*

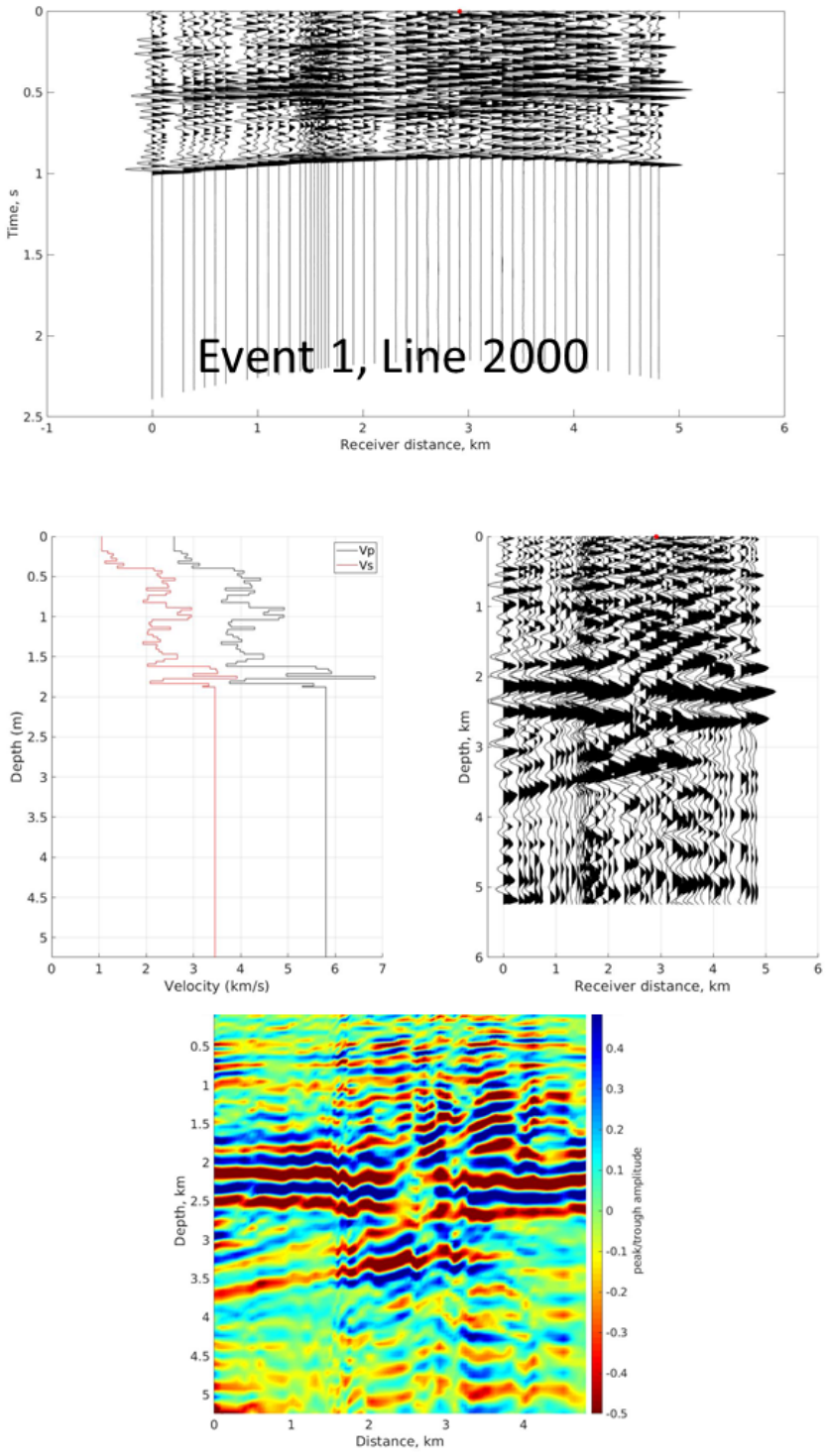

Fig. A1b: *Event 1, line 2000*

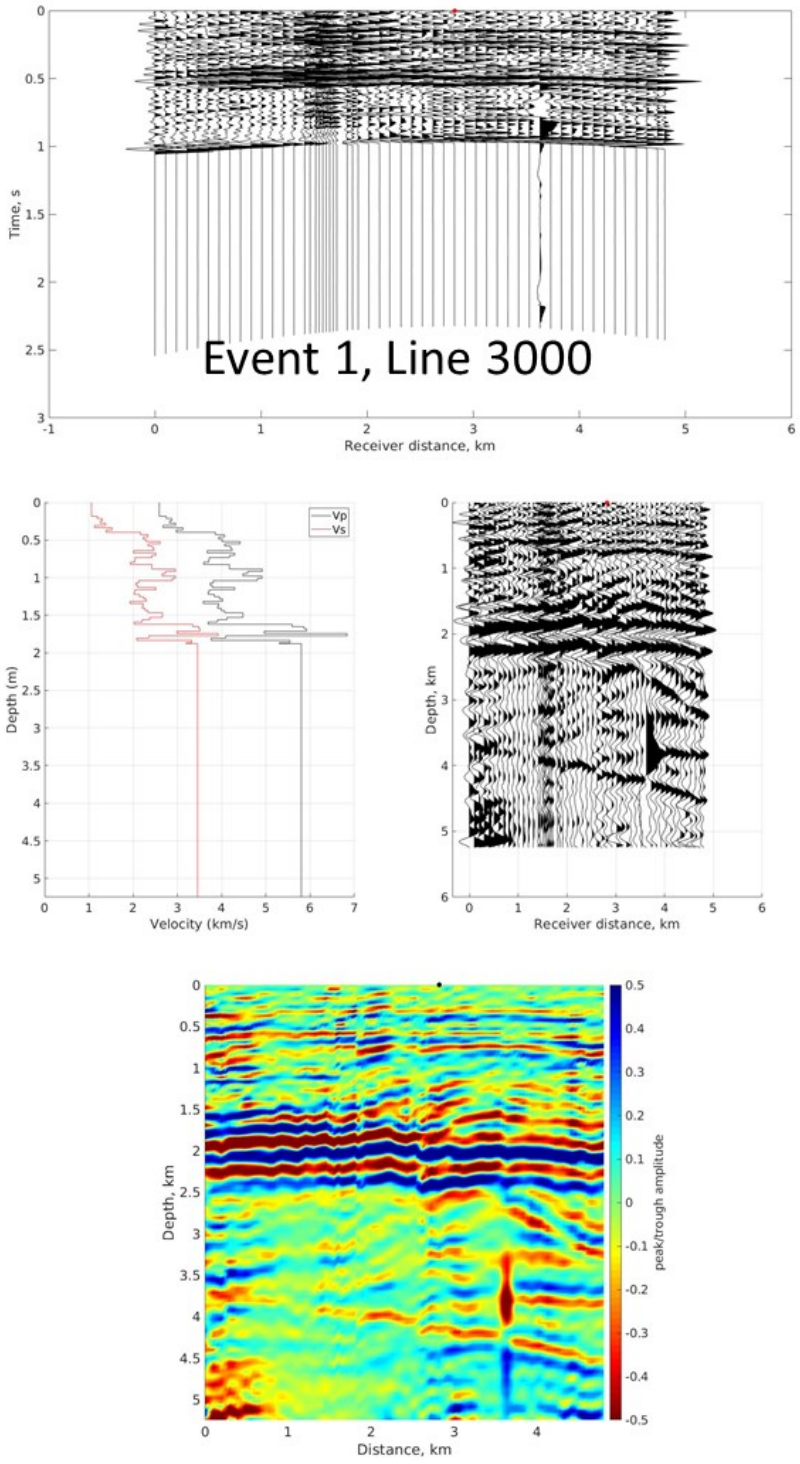

Fig. A1c: *Event 1, line 3000*

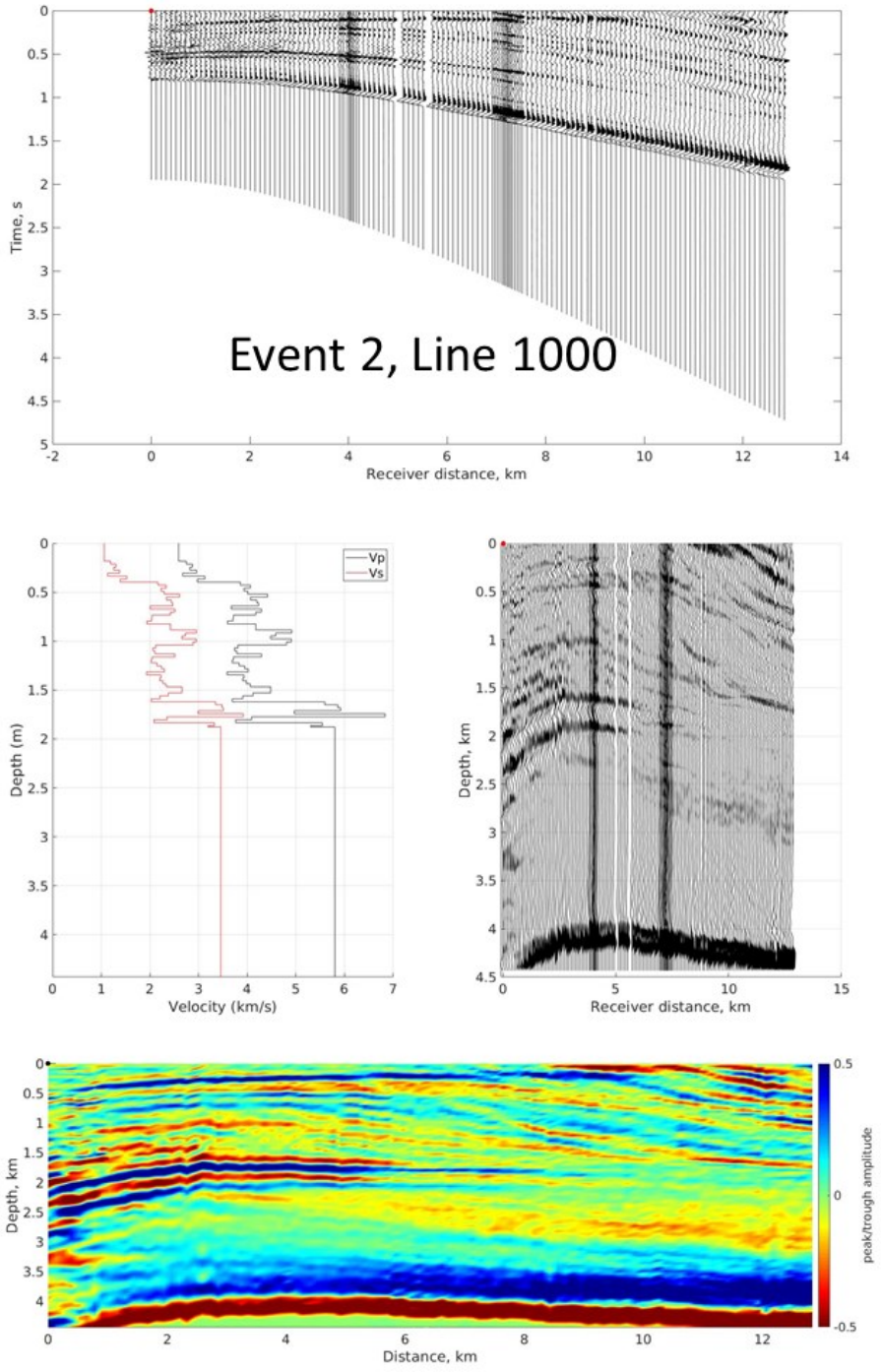

Fig. A2a: *Event 2, line 1000*

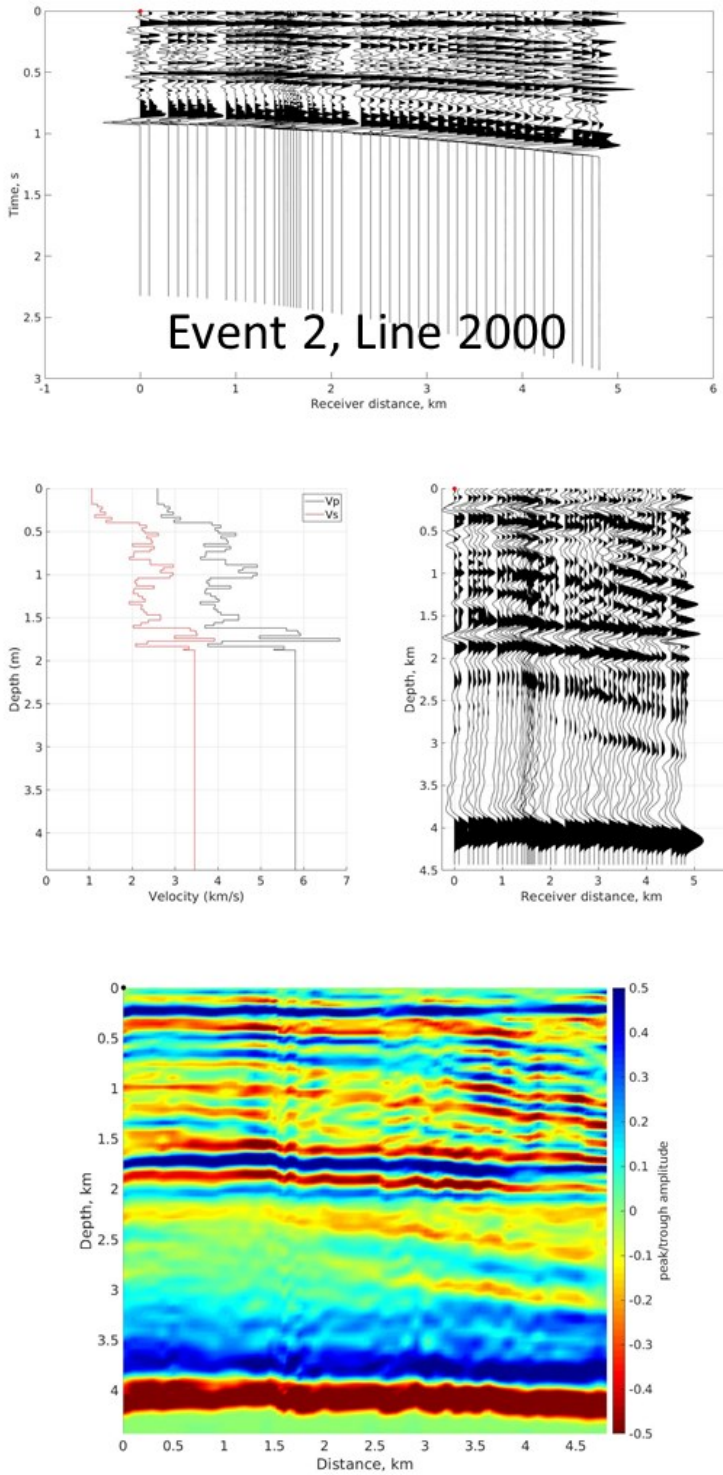

Fig. A2b: *Event 2, line 2000*

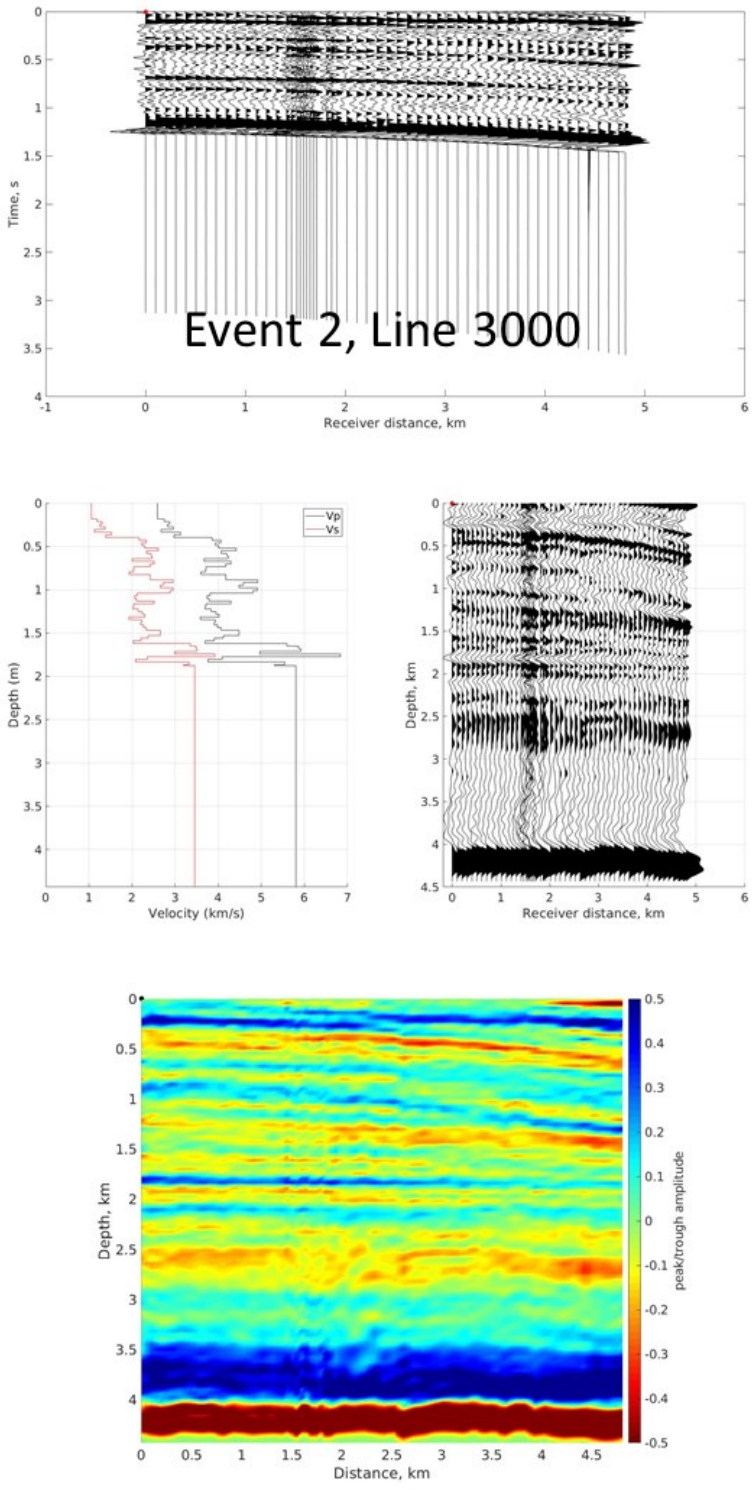

Fig. A2c: *Event 2, line 3000*

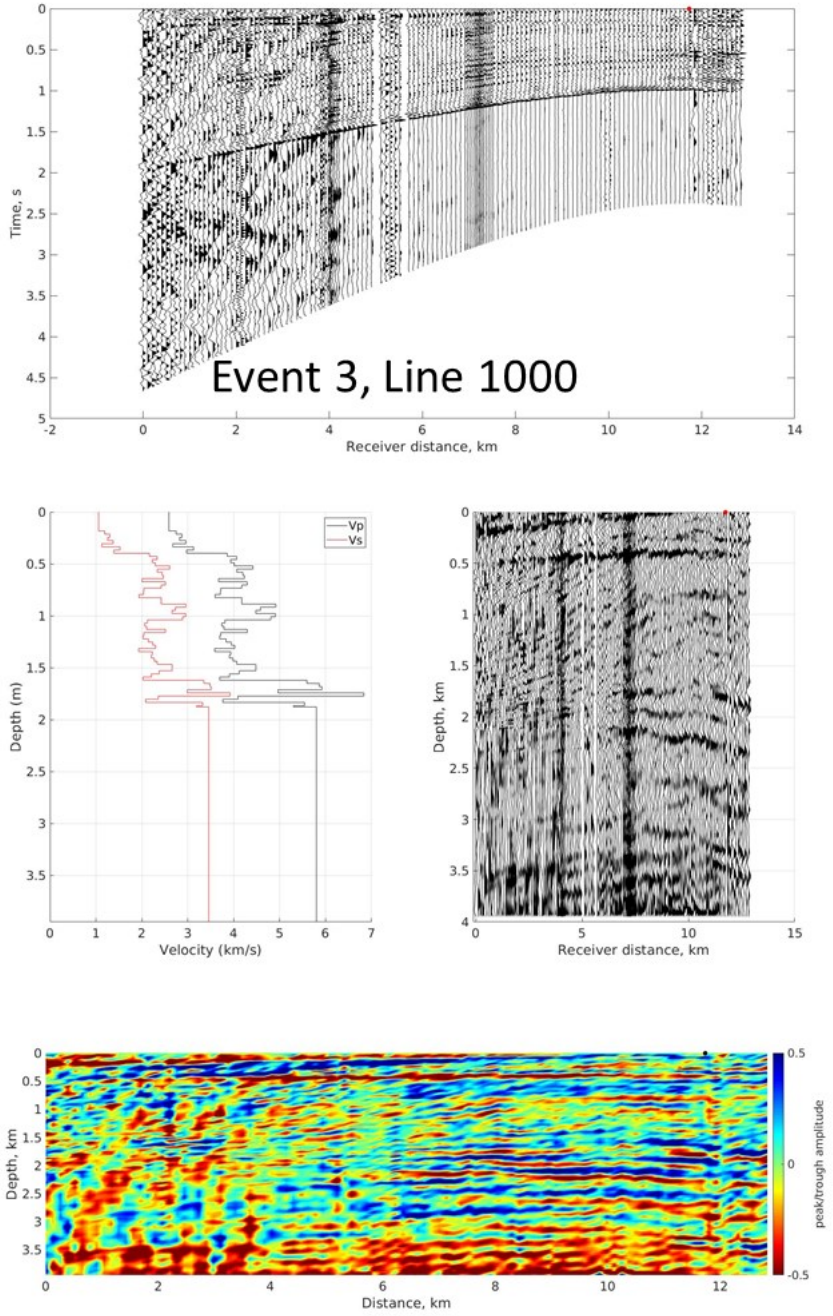

Fig. A3a: *Event 3, line 1000*

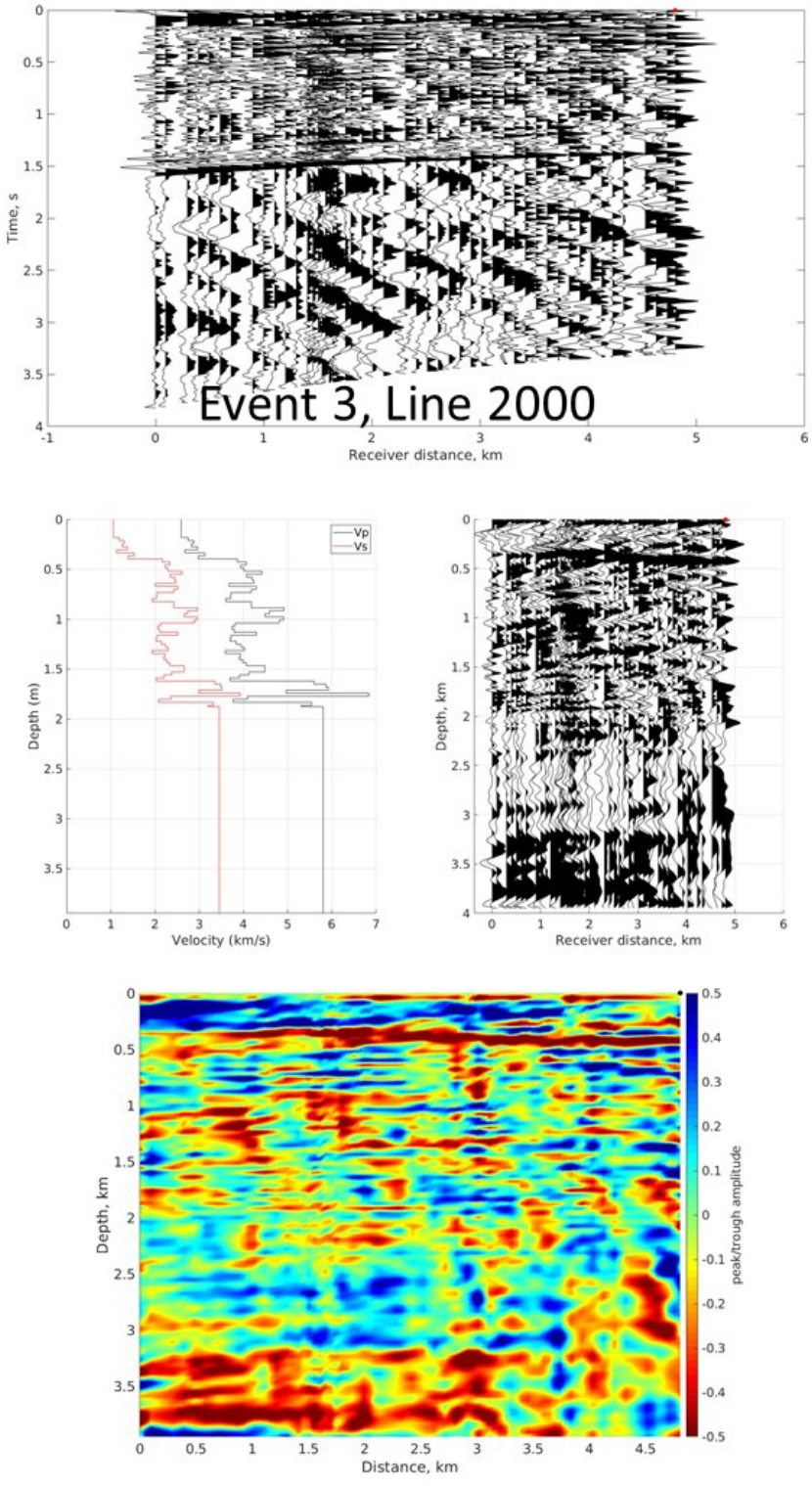

Fig. A3b: *Event 3, line 2000*

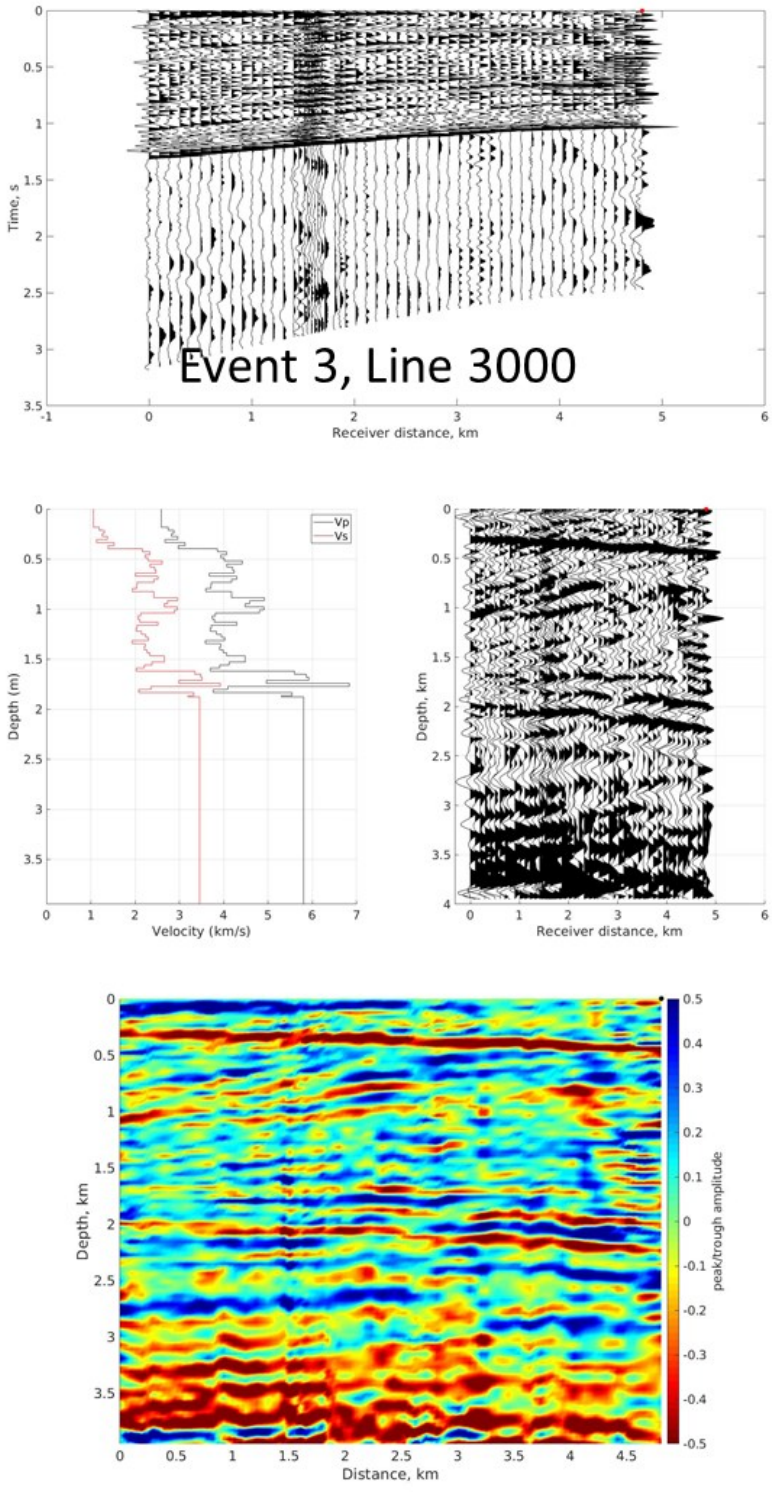

Fig. A3c: *Event 3, line 3000*

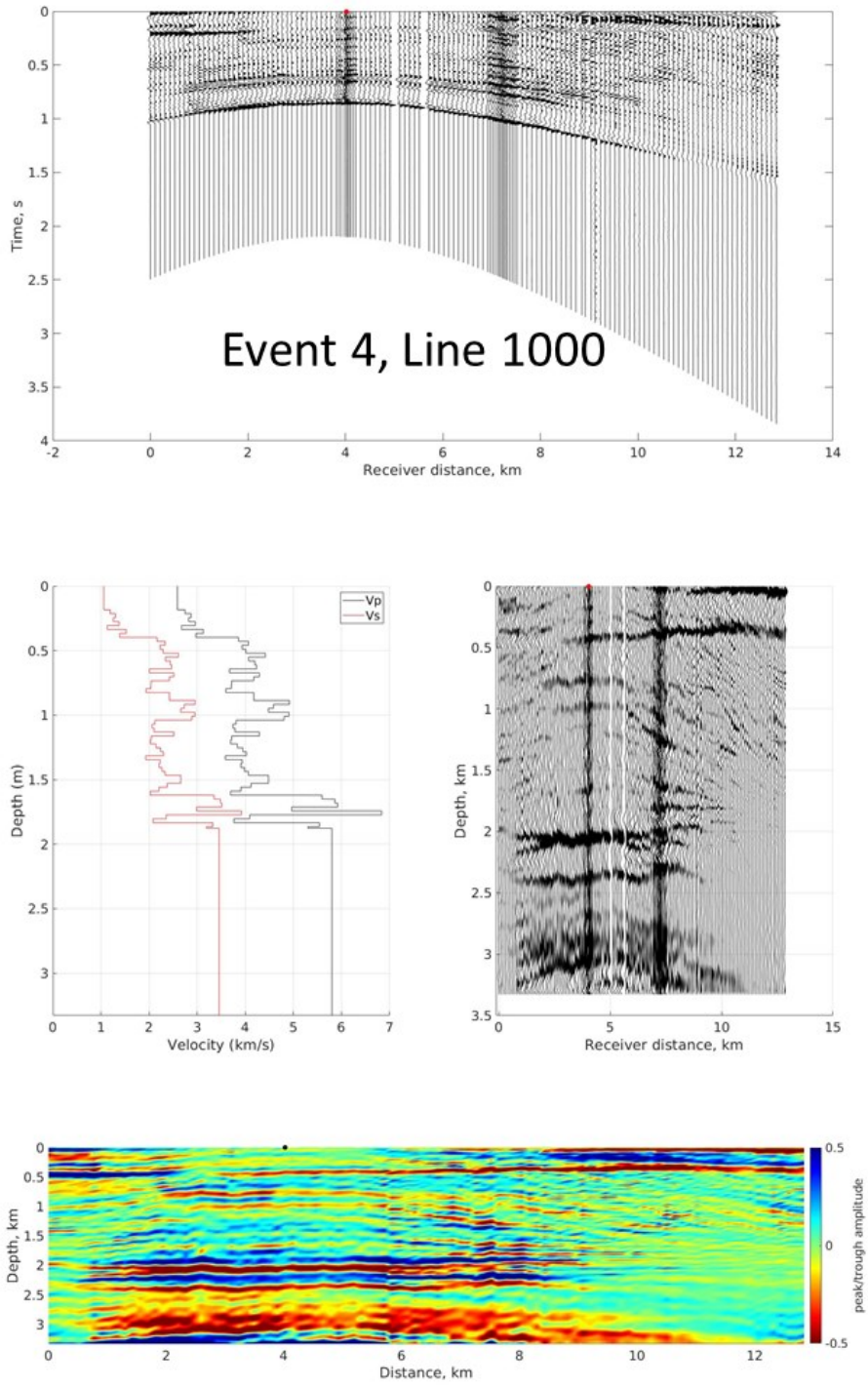

Fig. A4a: *Event 4, line 1000*

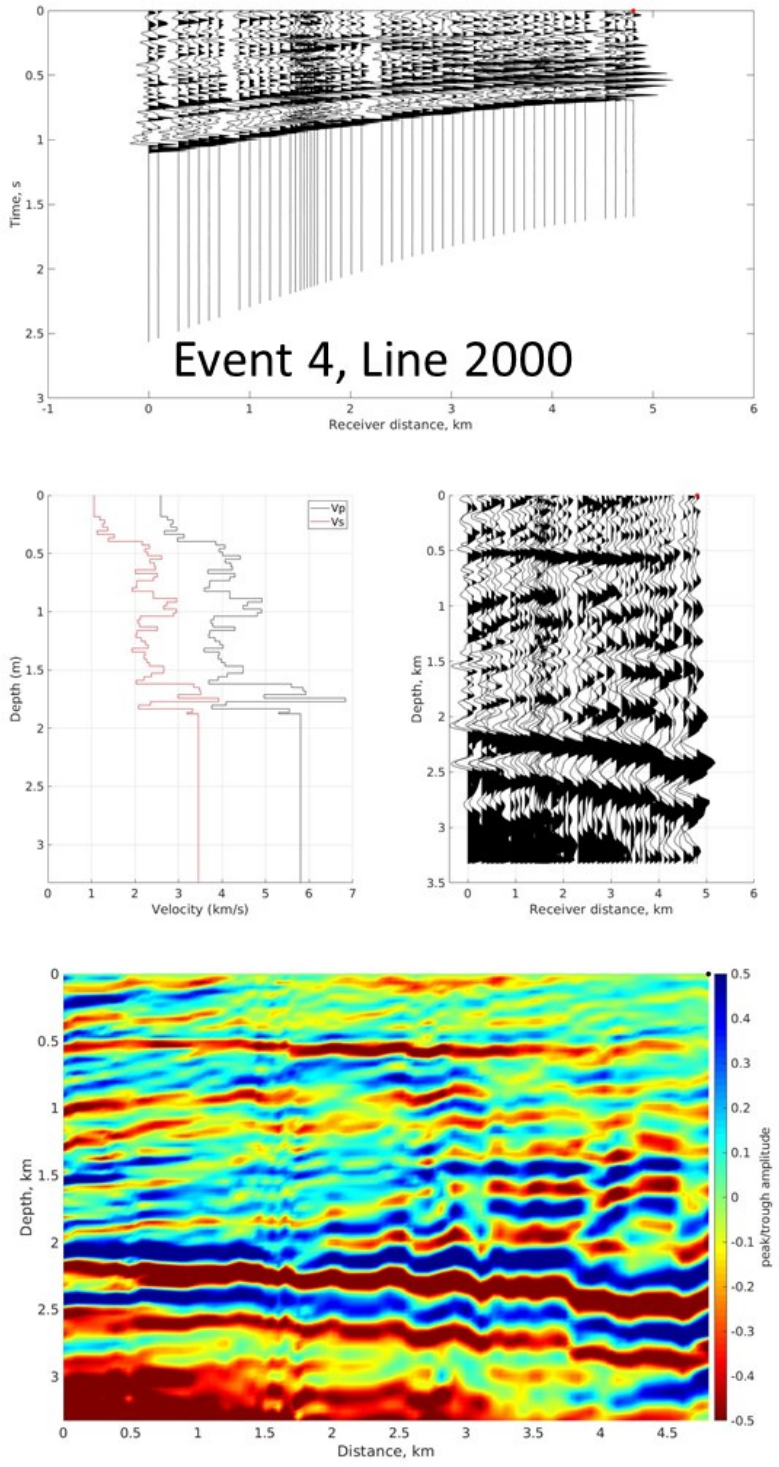

Fig. A4b: *Event 4, line 2000*

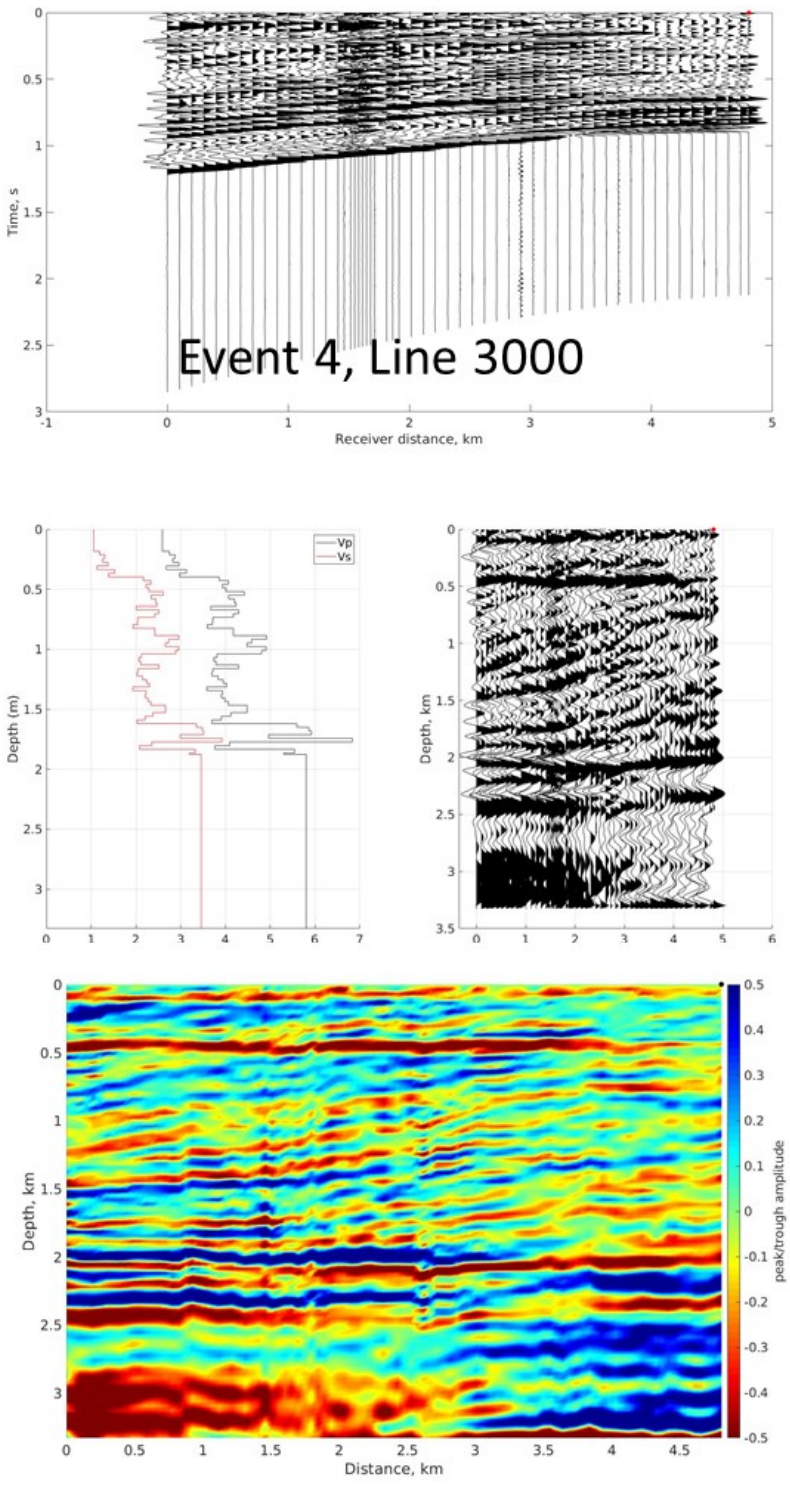

Fig. A4c: *Event 4, line 3000*

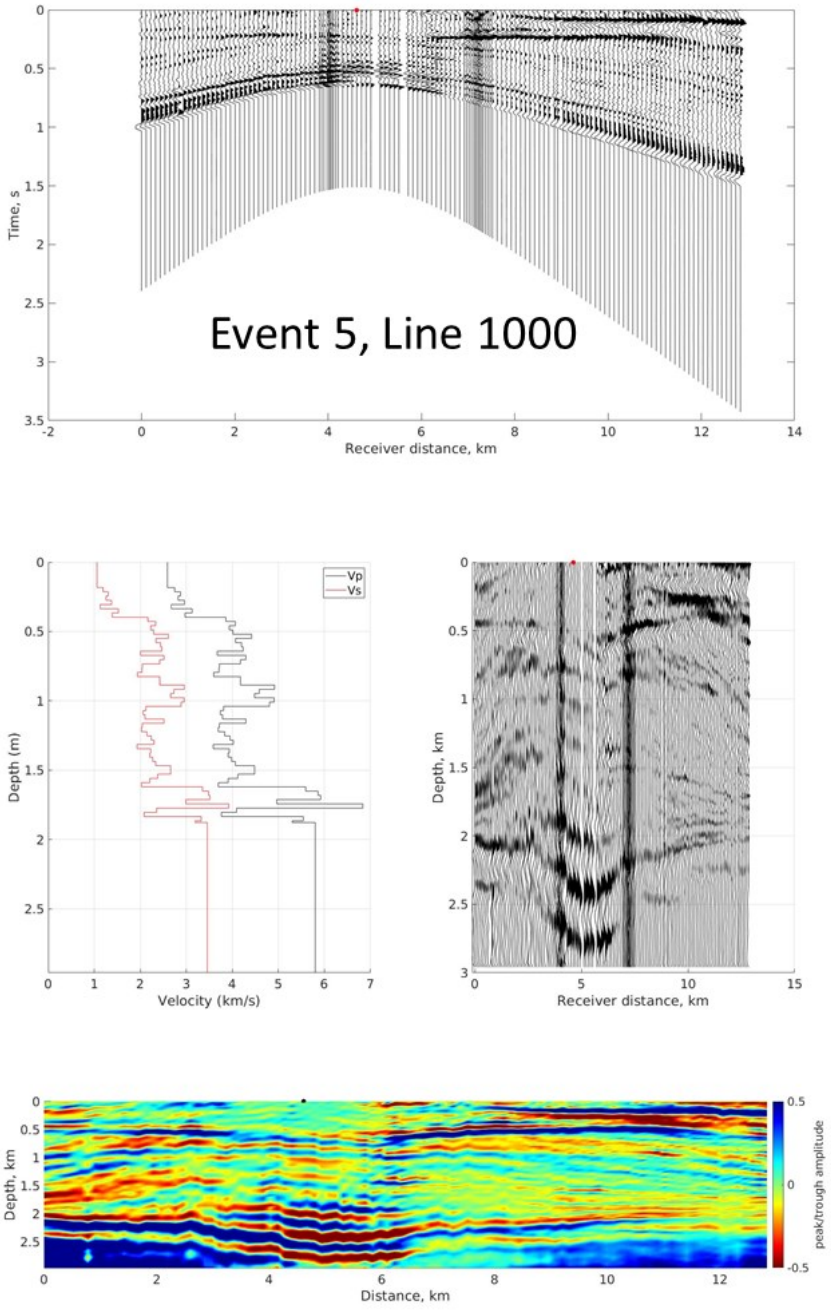

Fig. A5a: *Event 5, line 1000*

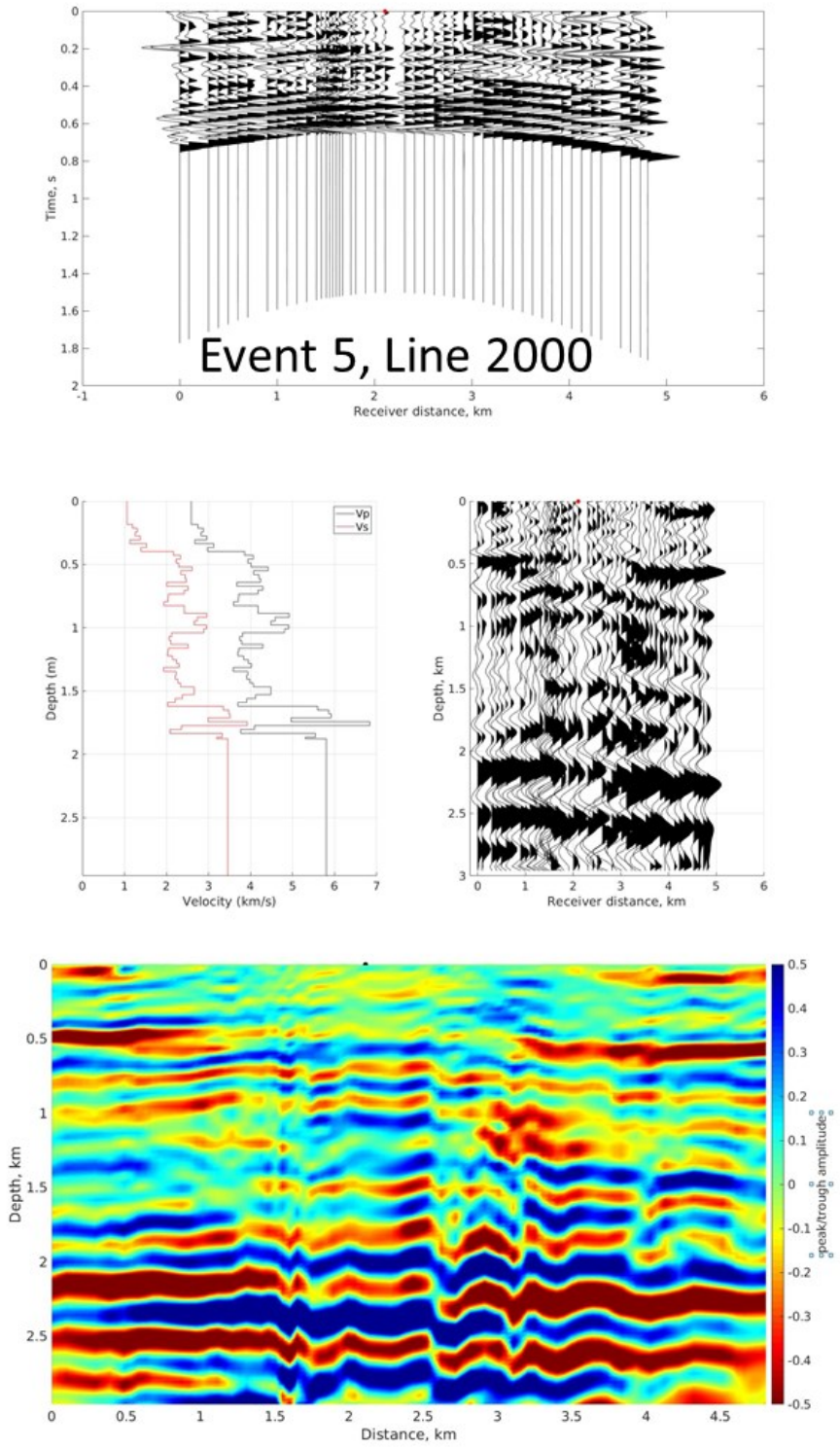

Fig. A5b: *Event 5, line 2000*

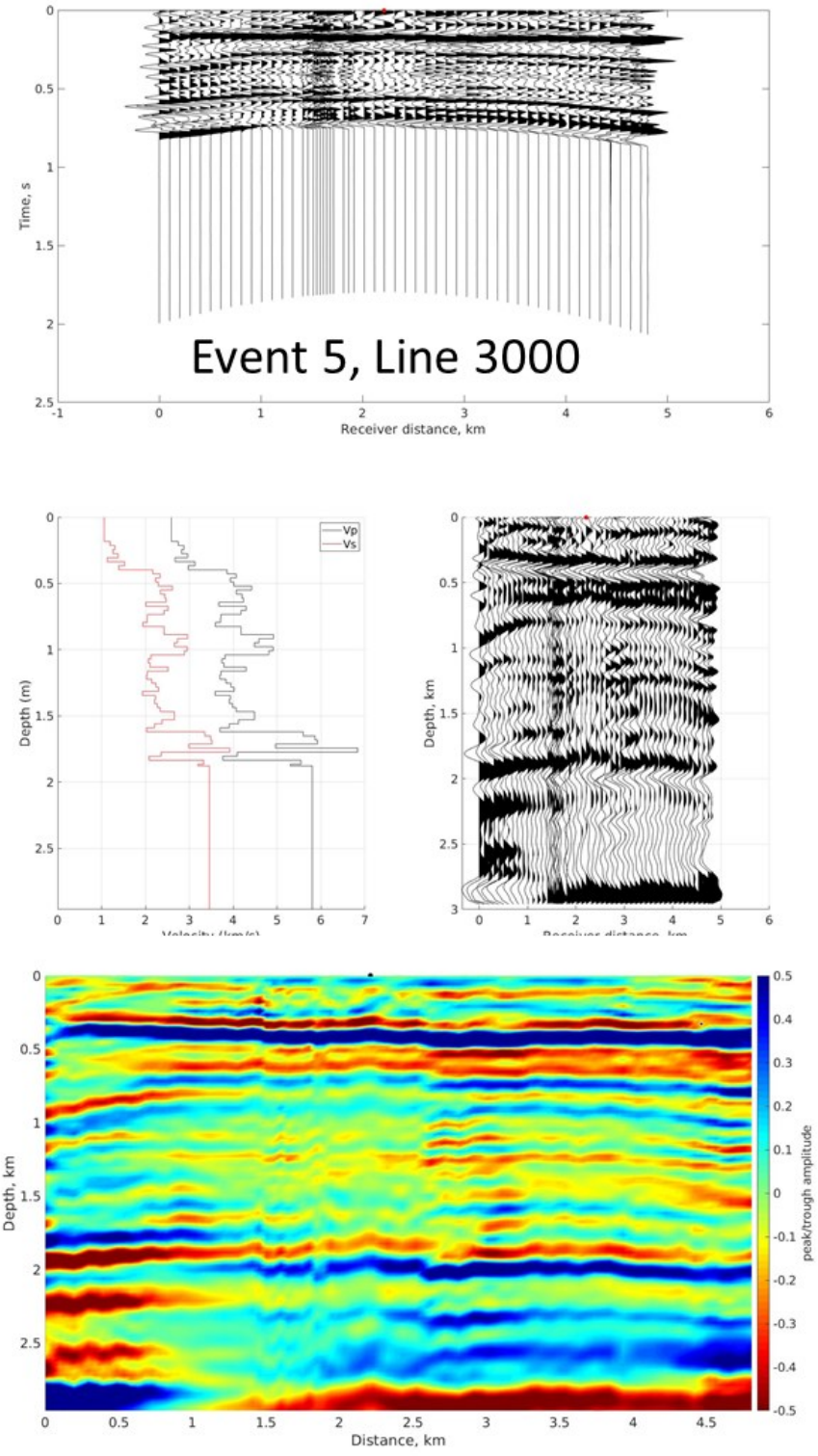

Fig. A5c: *Event 5, line 3000*